CHALMERS

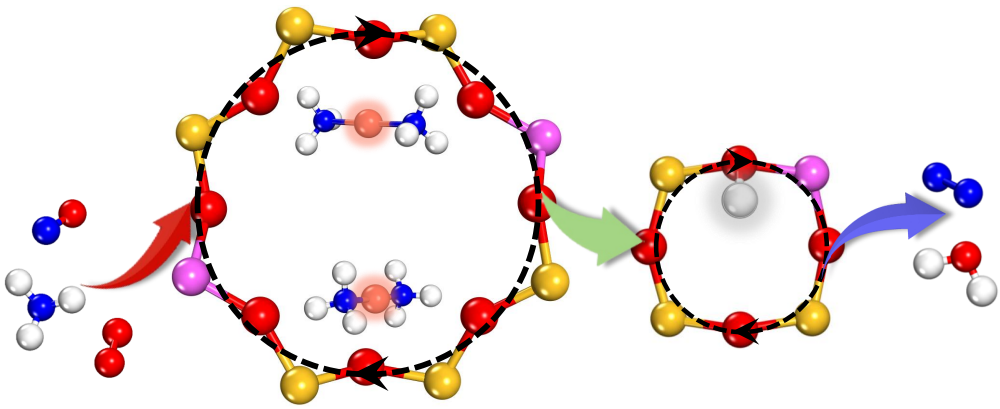

On the reaction mechanism for selective catalytic reduction of NO_x by NH_3 over Cu-zeolites

LIN CHEN

Department of Physics
CHALMERS UNIVERSITY OF TECHNOLOGY
Gothenburg, Sweden 2019

Thesis for the degree of Doctor of Philosophy

On the reaction mechanism for selective catalytic reduction of NO_x by NH_3 over Cu-zeolites

Lin Chen

CHALMERS

Department of Physics
Chalmers University of Technology
Gothenburg, Sweden 2019

On the reaction mechanism for selective catalytic reduction of NO_x by NH_3 over Cu-zeolites
Lin Chen
ISBN 978-91-7905-222-5

Department of Physics
Chalmers University of Technology
SE-412 96 Gothenburg
Sweden
Telephone: +46 (0)31-772 1000

Cover:
A schematic picture of the reaction mechanism for low-temperature NH_3-SCR over Cu-CHA

Printed at Chalmers Digitaltryck
Gothenburg, Sweden 2019

On the reaction mechanism for selective catalytic reduction of NO_x by NH_3 over Cu-zeolites

Lin Chen
Department of Physics
Chalmers University of Technology

Abstract

Nitrogen oxides (NO_x) are major pollutants from combustion processes, being corrosive and hazardous to human health. The main technology for exhaust aftertreatment of NO_x emitted from diesel engines is selective catalytic reduction with ammonia as reducing agent (NH_3-SCR). Among a range of catalysts for NH_3-SCR, copper-exchanged zeolites are efficient with high activity and selectivity combined with good hydrothermal stability. Zeolites are crystalline microporous aluminosilicates constructed by corner-sharing SiO_4 and AlO_4 tetrahedra. Replacement of a four-valent Si by a three-valent Al gives the framework a negative charge, which is compensated by a cation. The cation in the case of copper exchanged zeolites is Cu(I) or Cu(II).

In this thesis, the reaction mechanism for NH_3-SCR over copper-exchanged zeolites with CHA framework (Cu-CHA) has been studied through density functional theory in combination with *ab initio* thermodynamics and molecular dynamics. Firstly, the character of the active site for NH_3-SCR over Cu-CHA under typical reaction conditions has been investigated. It is found that the Cu(I)-ion is preferably solvated by two NH_3 ligands forming a linear $Cu(NH_3)_2^+$ complex under low-temperature operating conditions. The storage of NH_3 in the $Cu(NH_3)_2^+$ complex is consistent with measured features from NH_3 temperature-programmed desorption. Moreover, the linear $Cu(NH_3)_2^+$ complex is found to be important for solid-state ion exchange of Cu(I) into zeolites, which is one strategy for zeolite functionalization.

Secondly, a complete reaction mechanism for low-temperature NH_3-SCR over Cu-CHA has been explored. The reaction is found to proceed in a redox manner via alternating Cu(I) and Cu(II) oxidation states. A pair of $Cu(NH_3)_2^+$ complexes is found to be required for O_2 activation in similarity to O_2 activation in homogeneous catalysis. The potential energy surface for O_2 dissociation is found to depend strongly on the choice of the exchange-correlation functional. The PBE+U approach together with van der Waals corrections is found to provide a reasonable, simultaneous accuracy of the different bonds in the system. Based on the fact that Cu(I) is solvated and the need of complex pairs for O_2 activation, two possible reaction cycles for low-temperature NH_3-SCR are proposed. The reaction is suggested to proceed in a multi-site fashion over both copper-sites and Brønsted acid sites.

The proposed mechanism highlights the similarities between low-temperature NH_3-SCR over Cu-CHA and homogeneous liquid-phase catalytic reactions and provides a solid basis for future improvements of Cu-exchanged zeolites for NH_3-SCR.

Keywords: NH_3-SCR, Cu-CHA, Cu-SSZ-13, O_2-activation, Al-distribution, DFT

List of Publications

The thesis is based on the following appended papers:

I.
Mechanism for solid-state ion exchange of Cu into zeolites
L. Chen, J. Jansson, M. Skoglundh and H. Grönbeck
The Journal of Physical Chemistry C, **120** (2016), 29182–29189

II.
Activation of oxygen on $(NH_3\text{-}Cu\text{-}NH_3)^+$ in NH_3-SCR over Cu-CHA
L. Chen, H. Falsig, T.V.W. Janssens and H. Grönbeck
Journal of Catalysis, **358** (2018), 179–186

III.
Effect of Al-distribution on oxygen activation over Cu–CHA
L. Chen, H. Falsig, T.V.W. Janssens, J. Jansson, M. Skoglundh and H. Grönbeck
Catalysis Science & Technology, **8** (2018), 2131–2136

IV.
Interpretation of NH_3-TPD profiles from Cu-CHA using first-principles calculations
L. Chen, T.V.W. Janssens, M. Skoglundh and H. Grönbeck
Topics in Catalysis, **62** (2019), 93–99

V.
A comparative test of different density functionals for calculations of NH_3-SCR over Cu-Chabazite
L. Chen, T.V.W. Janssens, and H. Grönbeck
Physical Chemistry Chemical Physics, **21** (2019), 10923–10930

VI.
A complete multi-site reaction mechanism for low-temperature NH_3-SCR over Cu-CHA
L. Chen, T.V.W. Janssens, P.N.R. Vennestrøm, J. Jansson, M. Skoglundh and H. Grönbeck
Submitted

VII.
Direct evidence of NH_3-promoted O_2 activation over Cu-CHA at low temperature
X.T. Wang, L. Chen, P.N.R. Vennestrøm, T.V.W. Janssens, J. Jansson, H. Grönbeck and M. Skoglundh
In manuscript

Related publications not included in this thesis:

Monte carlo potential energy sampling for molecular entropy in zeolites
M. Jørgensen, L. Chen and H. Grönbeck
The Journal of Physical Chemistry C, **122** (2018), 20351–20357

My contributions to the publications

Paper I
I performed all the calculations and wrote the first draft of the paper, which was finalized together with my coauthors.

Paper II
I performed all the calculations and wrote the first draft of the paper, which was finalized together with my coauthors.

Paper III
I performed all the calculations and wrote the first draft of the paper, which was finalized together with my coauthors.

Paper IV
I performed all the calculations and wrote the first draft of the paper, which was finalized together with my coauthors.

Paper V
I performed all the calculations and wrote the first draft of the paper, which was finalized together with my coauthors.

Paper VI
I performed all the calculations and wrote the first draft of the paper, which was finalized together with my coauthors.

Paper VII
I performed all the calculations and wrote the first draft of the manuscript together with Xueting Wang, which was finalized together with other coauthors.

Contents

Chapter 1

Introduction

Ever since its discovery in the late eighteenth century, catalysis has played an essential role in the society. Catalysts are crucial in a range of areas such as production of chemicals and fertilizers, and for fuel synthesis and emission control. A catalyst speeds up a chemical reaction without being consumed such that it is available for multiple reaction cycles. Catalysts are generally classified as either homogeneous or heterogeneous.[1] In homogeneous catalysis, the reactants and the products are in the same phase as the catalyst. In heterogeneous catalysis, the catalyst is in a different phase from the reactants and products. A heterogeneous catalyst is usually in solid phase whereas the reactants and products are gaseous or liquid.[2] Figure 1.1 shows a typical free energy diagram for a heterogeneous catalytic reaction compared with its non-catalyzed reaction and a side reaction. With a catalyst, it is possible to reduce the energy required to perform the reaction. The reduction of the barrier is generally accomplished by opening up alternative reaction paths. As is shown in Figure 1.1, it is also possible to have unwanted side reactions, where in Figure 1.1 product D might be produced instead of product C. However, in this case, the rate of the unwanted reaction might be low thanks to a higher barrier. This exemplifies the selectivity of a catalyst, which steers the reaction to particular products. The selectivity is generally created by high barriers for unwanted reactions whereas the wanted reactions have low barriers. Selective catalytic reduction of nitrogen oxides to N_2 and H_2O in oxygen excess is an important example and the main subject of this thesis.

1.1 NO_x abatement

Fossil resources, such as oil, coal and natural gas, have been the primary energy sources over the last two hundred years. The fossil energy sources are burned to produce electricity, or refined for use as fuels in transportation. The use of fossil energy sources is convenient thanks to the high energy density. However, combustion also produces several hazardous pollutants, such as carbon monoxide (CO), nitrogen oxides (NO_x), sulfur oxides (SO_x) and hydrocarbons (HCs).[3] The transport sector is the largest contributor of these pollutants to the atmosphere.[4] The contribution from different sectors to emissions of NO_x is shown in Figure 1.2. NO_x is primarily produced from the reaction of nitrogen and oxygen in air at high temperature during combustion.[5] NO_x release from transports is almost half of the total NO_x emissions. Particularly, lean-burn diesel engines contribute with the major part of NO_x emissions.[6]

NO_x, primarily NO and NO_2, emissions need to be controlled as NO_x can interact with water, oxygen and other compounds in the atmosphere to form acid rain. The nitrate species that result from NO_x can also cause haze. Therefore, considerable efforts are

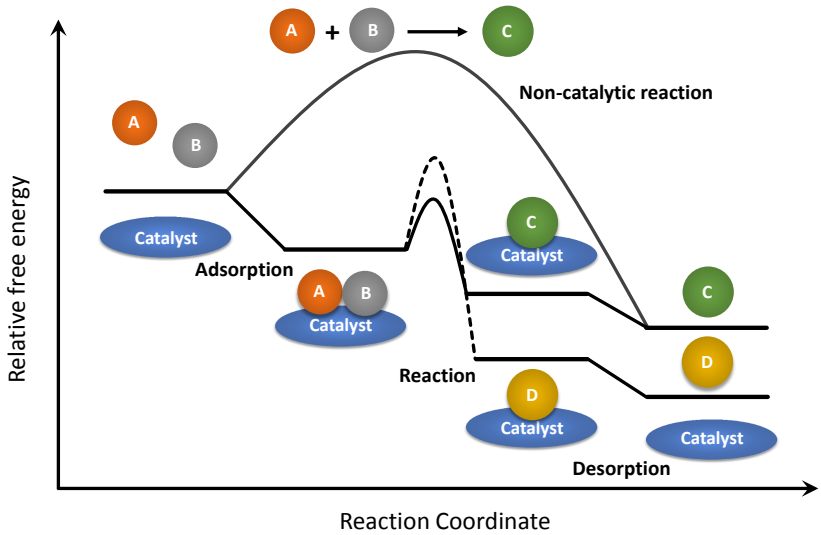

Figure 1.1: Potential energy diagram for a heterogeneous catalytic reaction A + B → C compared with the non-catalytic reaction and an unwanted side reaction A + B → D.

made to minimize NO_x emissions either by combustion control or by abatement control using aftertreatment systems. The development of NO_x-aftertreatment systems with high activity and durability is enforced by increasingly stricter legislations.[7] For stoichiometric gasoline engine exhausts, the pollutants are mainly unburned HCs, CO, and NO_x, which can be effectively converted to N_2, CO_2 and H_2O through a series of oxidation and reduction steps by the three-way catalyst technology.[8–10] However, the three-way catalyst achieve simultaneous conversion of HCs, CO, and NO_x only if the air/fuel ratio is close to stoichiometric.[10] When the air/fuel ratio is low (rich mode), CO and HCs can not be completely oxidized due to the insufficient supply of oxygen.[11] Instead, when the air/fuel ratio is high (lean mode), the reduction of NO_x will be suppressed by oxygen.[11] Thus, the three-way catalyst is not suitable for NO_x reduction of lean-burn diesel engine exhausts as the noble metals (such as Pt or Pd) exhibit a poor selectivity for NO_x reduction in oxygen excess.[9] Up to now, two main approaches are used for NO_x abatement in the exhausts of diesel-engine vehicles, namely NO_x storage reduction (NSR)[12;13] and selective catalytic reduction (SCR) using either HCs or NH_3 as reducing agents.[14;15]

The NSR technology is used together with rich/lean operation of the engine. During long lean operation intervals, the NO_x in the exhaust is stored on the catalyst as nitrate or nitrite species, and during short rich operation intervals, the stored species are reduced to nitrogen.[13] However, there are several drawbacks with the NSR technology, such as low activity during low temperatures (below $\sim 200°C$), fuel penalty as the engine needs rich operation, dependence on the noble metals and sensitivity to poisons.[12] Instead, the selective catalytic reduction (SCR) of NO_x by a reducing agent (HCs or NH_3) has emerged as the main approach for NO_x abatement connected to lean burn engines.[14;16;17]

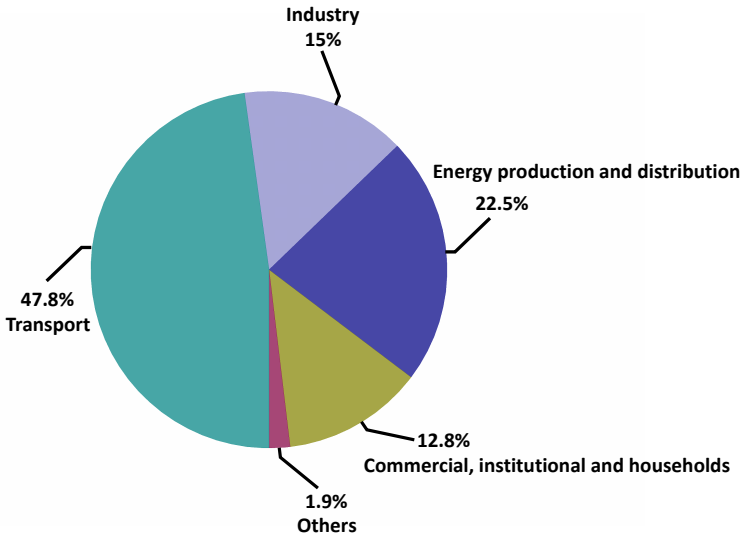

Figure 1.2: The contributions from different sectors to emissions of nitrogen oxides in 2011. Data are taken from Ref. [4].

Particularly, SCR using NH_3 as the reducing agent (NH_3-SCR) shows good performance. The HC-SCR technology has issues with fuel penalty and lower hydrothermal stabilities during the practical vehicle exhaust conditions.[16]

1.2 Selective catalytic reduction of NO_x by NH_3

The NO_x emissions from current diesel-engines consist typically of 95% NO and 5% NO_2. Reduction of NO with NH_3 will therefore mainly follow the so-called "standard" NH_3-SCR reaction:[18]

$$4NH_3 + 4NO + O_2 \rightarrow 4N_2 + 6H_2O \tag{1.1}$$

When the ratio between NO and NO_2 is close to 1:1, the reaction can follow the so-called "fast" NH_3-SCR reaction:[18]

$$4NH_3 + 2NO + 2NO_2 \rightarrow 4N_2 + 6H_2O \tag{1.2}$$

If the NO:NO_2 ratio is below 0.5, an SCR reaction with only NO_2 may take place:[5]

$$8NH_3 + 6NO_2 \rightarrow 7N_2 + 12H_2O \tag{1.3}$$

The latter reaction is known to proceed at slower rate than the fast NH_3-SCR reaction and sometimes also slower than the standard NH_3-SCR reaction.[15] Thus, the reaction with only NO_2 is often referred to as the "slow" NH_3-SCR reaction.

The three Reactions (1.1 - 1.3) are the desired NH_3-SCR reactions and the catalyst should steer the processes in these directions. Due to the excess of the oxygen, there is, however, a possibility of several unwanted reactions. The oxidation of NH_3 to NO or N_2O are possible alternative reaction paths.[15;19] The oxidation of NH_3 by O_2 (Reaction 1.4-1.6) is undesirable because, on one hand, less NH_3 will be available for reduction of NO_x and, on the other hand, it produces NO or the greenhouse gas N_2O (Reaction 1.6). N_2O can also be formed by the reaction between NH_3 and NO_2 (Reaction 1.7 and 1.8).[18]

$$4NH_3 + 3O_2 \rightarrow 2N_2 + 6H_2O \tag{1.4}$$

$$4NH_3 + 5O_2 \rightarrow 4NO + 6H_2O \tag{1.5}$$

$$2NH_3 + 2O_2 \rightarrow N_2O + 3H_2O \tag{1.6}$$

$$2NH_3 + 2NO_2 \rightarrow N_2O + N_2 + 3H_2O \tag{1.7}$$

$$6NH_3 + 8NO_2 \rightarrow 7N_2O + 9H_2O \tag{1.8}$$

1.3 Catalysts for NH_3-SCR

The typical temperature of diesel exhausts from trucks is below 300 °C and the catalyst will be exposed mainly to exhausts with a temperature of about 200 °C when driving on highway.[20;21] Due to many competing reactions during NH_3-SCR conditions, the research and development have been intense to find suitable catalysts. In addition to high activity for NH_3-SCR at the typical reaction conditions, the catalyst should also have a selectivity to avoid the undesirable side reactions.

For the standard NH_3-SCR reaction (Reaction 1.1), the catalyst should allow for adsorption and dissociation of O_2. The catalyst should, moreover, allow for NO and NH_3 adsorption, and N-N coupling to form N_2. The N atoms in N_2 originate from both NO and NH_3 during standard SCR.[22] The catalyst should not promote NH_3 oxidation reactions (Reactions 1.4-1.6) by the coupling of NH_3 and O_2. An additional property of the catalyst is that it should prevent the formation of N_2O.

The first property requires that the catalyst has a redox ability. The second and third properties imply that NH_3 should not react with activated oxygen species when NH_3 is sequentially dehydrogenated. It is not very difficult to satisfy the first property as many transition metals (for example Pt, Pd, Fe, V and Cu) have redox ability. However, based on the second and third properties, extended surfaces of metals can be ruled out as SCR catalysts because of high probabilities for dehydrogenated NH_3 species (N, NH and NH_2) to react with oxygen giving rise to NH_3 oxidation. Actually, precious metals, in particular Pt, are widely used as NH_3 slip catalysts as they show high activity for NH_3 oxidation.[23;24] Therefore, isolated active sites have been considered for NH_3-SCR catalysts.

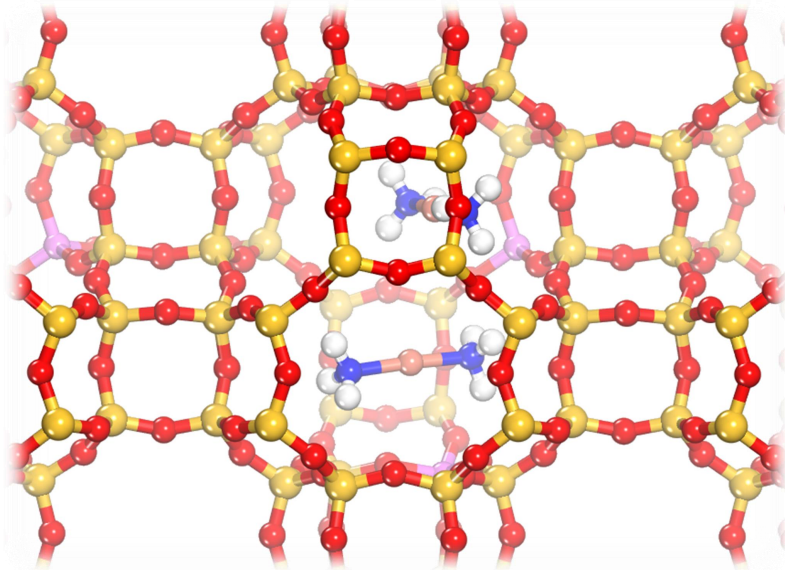

Figure 1.3: Fragment of a zeolite with CHA framework with two Al located per large cage. NH_3 solvated Cu(I) complexes ($Cu(NH_3)_2^+$) are counter cations that balance the charge. Color code: copper (pink), aluminum (purple), nitrogen (blue), silicon (yellow), oxygen (red) and hydrogen (white).

Metal-exchanged zeolites are one of the choices for NH_3-SCR. In these catalysts, the metal ions are highly dispersed in porous zeolite structures, which creates isolated sites for the reaction. Zeolites are crystalline, microporous aluminosilicate materials constructed by corner-sharing SiO_4 or AlO_4 tetrahedra.[25] The difference in oxidation states between silicon and aluminum (Si^{4+} versus Al^{3+}) requires one counter ion per Al^{3+} in the zeolite framework, for example a proton H^+, to maintain charge neutrality. The compensation of the charge by a proton generates Brønsted acidity.[26] Different metal cations are introduced into zeolites by ion-exchange methods, which is generally the procedure to functionalize zeolites. The exchanged metal cations create Lewis acidity of the catalyst. There are several types of framework structures of zeolites used for NH_3-SCR, such as *BEA[27], MFI[28] and CHA[29]. However, the issue with unburned hydrocarbons in large- and medium-pore zeolites (*BEA and MFI)[16] has motivated the exploration of small-pore zeolites. Indeed, metal-exchanged zeolites with the CHA framework structure (particularly Cu-SSZ-13) have shown high activity for NH_3-SCR with NO_x conversion rates of 90-100% and high selectivity with low NH_3 oxidation rate combined with high hydrothermal stability.[16] Figure 1.3 shows a view of a fragment of a zeolite with CHA framework with two Al located per cage. In this example, complexes of NH_3 solvated Cu(I), $Cu(NH_3)_2^+$, are the counter cations to balance the negative charge. This solvated character of the active site has been found to be important for the NH_3-SCR reactions at low temperature (below 200 °C)[30;31] and is similar to the active sites in enzymatic catalysis.[32]

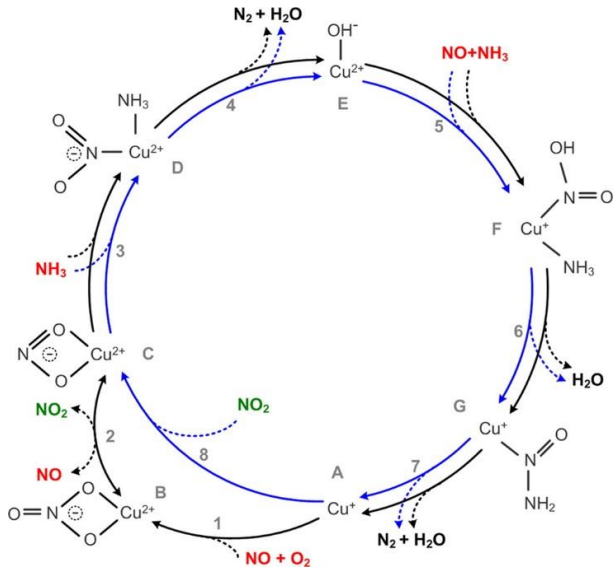

Figure 1.4: A tentative reaction mechanism for the SCR reaction in a Cu-zeolite proposed by Janssens *et al.*[22] This figure is reprinted with permissions from Ref. [22]. Copyright (2015) American Chemical Society.

Vanadia supported on titania has for decades been used as a catalyst for NH_3-SCR.[33] On the vanadia surface, each vanadium ion is coordinated by oxygen atoms creating an isolated active site. The vanadium ion has the ability to change the oxidation state between V^{4+} and V^{5+}. However, this catalyst has poor hydrothermal stability and the selectivity decreases dramatically due to increased oxidation of NH_3 at high temperatures.[34] Other problems of vanadia include toxicity of volatile vanadia species and enhanced oxidation rate of SO_2 to SO_3. Note that the zeotype Cu-SAPO-34, which has the CHA framework structure, has also been considered for NH_3-SCR. However, due to the lack of durability at low temperatures in the presence of moisture, Cu-SAPO-34 shows poor activity for low-temperature NH_3-SCR.[35] The reason has been attributed to the dealuminization by forming the Cu-aluminate like species, which is facilitated by water molecules.[35] Thus, copper-exchanged zeolites with the CHA framework structure (from here on denoted Cu-CHA) is presently the material of the choice for NH_3-SCR.

1.4 Objectives of this thesis

What is the reason for the simultaneous high activity and high selectivity of Cu-CHA for NH_3-SCR? The question is linked with the understanding of the reaction mechanism. Although this question is still under debate, the understanding of the NH_3-SCR mechanism over Cu-CHA has advanced significantly in recent years[22;30;31;36;37]. Figure 1.4 shows a tentative reaction mechanism proposed by Janssens *et al.*[22] It is established that the NH_3-SCR reaction proceeds via alternating reduction and oxidation steps. Cu ions are in

the reduction step reduced from Cu(II) to Cu(I), whereas Cu(I) is reoxidized to Cu(II) in the oxidation step.

By a combination of spectroscopy and first principles calculations, it has been shown that the copper ions are solvated by NH_3 under typical reaction conditions for NH_3-SCR below 250 °C.[36–39] Cu(I) is preferably solvated by two NH_3 ligands forming $Cu(NH_3)_2^+$, whereas $Cu(NH_3)_4^{2+}$ is preferred for Cu(II). Thus, the reaction mechanism in Ref. [22] needs to be further studied for low-temperature NH_3-SCR as the selected intermediates in the cycle were considered to be framework-bonded copper sites. The coordination of Cu to NH_3 makes the Cu species mobile and the understanding of the active sites in Cu-zeolites during NH_3-SCR reactions should be revised.

In this thesis, the character of the active site and the reaction mechanism for NH_3-SCR over Cu-CHA have been studied by theoretical approaches. The methods are described in detail in Chapter 2 and 3. Chapter 4 describes the character of the active site under typical reaction conditions. Based on the state of the active site and the reaction mechanism for O_2 activation, a complete multi-site reaction mechanism is proposed in Chapter 5. The thesis is concluded by some general comments in Chapter 6.

Chapter 2

Electronic structure calculations

Understanding the electronic structure of a reaction is fundamental. For a catalyst, it is the redistribution of electrons that enable bond breaking and bond making. In this chapter, methods of electronic structure calculations, in particular, density functional theory will be reviewed. The approaches to perform electronic structural calculations in practice will also be discussed.

2.1 The Schrödinger equation

The electrons move much faster than the nucleus as the mass of a proton is at least 1840 times larger than that of an electron. Therefore, for a given set of electrons moving in the field of a set of nuclei, it is possible to treat the electrons as moving in a stationary external potential generated by the nuclei. This is the, so-called, Born-Oppenheimer approximation.[40] Within this approximation, the energy of the electrons can be expressed as a function of positions of the nuclei.

The basic equation to describe an electron is the Schrödinger equation, where an electron is represented by a wave function ψ. The physical interpretation of the wave function is that the square modulus ($|\psi|^2$) represents the probability density for the electron to be found within some region of space.

The time-independent, non-relativistic Schrödinger equation is[41]

$$\hat{H}\Psi = E\Psi. \tag{2.1}$$

Here, $\hat{H}$ is the Hamilton operator, Ψ is the many-electron wave function and E is the total energy. The Hamilton operator for the electrons is the sum of the kinetic and potential energy operators, which can be written in atomic units[1] as:

$$\hat{H} = -\frac{1}{2}\sum_i \nabla^2_{\mathbf{r}_i} + \frac{1}{2}\sum_{\substack{i,j \\ i\neq j}} \frac{1}{|\mathbf{r}_i - \mathbf{r}_j|} - \sum_{I,i} \frac{Z_i}{|\mathbf{R}_\mathrm{I} - \mathbf{r}_i|} \tag{2.2}$$

The three terms correspond to the kinetic energy of the electrons, the potential energy of electron-electron Coulomb interaction and the potential energy of nucleus-electron Coulomb interaction, respectively. Solving the electronic Schrödinger equation gives the corresponding potential energy surface (PES) with respect to the positions $\mathbf{R}_\mathrm{I}$ of the nuclei. Note that the wave functional can also be evolved in time according to the time-dependent Schrödinger equation.

[1] Atomic units (a.u.) form a system of natural units which is convenient for atomistic calculations. The mass of electron m_e, charge of an electron e, reduced Planck's constant $\hbar$ and Coulomb force constant $4\pi\varepsilon_0$ are put to unity when atomic units are used.

The electronic Schrödinger equation can only be solved exactly for one-electron systems like the hydrogen atom. Thus, the wave function is generally unknown for multi-electron system and has to be approximated. One starting point for the solutions to multi-electron systems is the Hartree-Fock method.[42;43] In this method, the interactions from the other electrons are taken into account in a mean-field fashion. Because electrons are fermions and obey the Pauli exclusion principle, the wave function must change sign if the coordinates of two electrons are exchanged. Thus, the wave function must be antisymmetric with respect to coordinate exchange. This constraint can be satisfied by constructing a Slater determinant of one-electron wave functions.[43] By using a Slater determinant, the electron exchange energy in the Hartree-Fock approach is given by

$$E_{\mathrm{x}}^{\mathrm{HF}} = -\frac{1}{2}\sum_{i,j}\int\int \psi_i^*(\mathbf{r})\psi_j^*(\mathbf{r}')\frac{1}{|\mathbf{r}-\mathbf{r}'|}\psi_j(\mathbf{r})\psi_i(\mathbf{r}')d\mathbf{r}d\mathbf{r}'. \tag{2.3}$$

In a Hartree-Fock calculation, the one-electron wave functions are obtained by solving the Hartree-Fock one-electron equations, which for every i is:

$$\begin{aligned}[-\frac{1}{2}\nabla^2 - \sum_I \frac{Z_I}{|\mathbf{r}_i-\mathbf{R}_I|} + \sum_j \int \frac{|\psi_j(\mathbf{r}')|^2}{|\mathbf{r}-\mathbf{r}'|}d\mathbf{r}']\psi_i(\mathbf{r}) \\ -\sum_j \int \frac{\psi_j^*(\mathbf{r}')\psi_i(\mathbf{r}')}{|\mathbf{r}-\mathbf{r}'|}\psi_j(\mathbf{r})d\mathbf{r}' = \varepsilon_i\psi_i(\mathbf{r}).\end{aligned} \tag{2.4}$$

The third and fourth term is the electron-electron Coulomb and the exchange interaction, respectively. The N-electron wave functions are constructed by combining all the solutions of the Hartree-Fock one-electron equations in a single Slater determinant. As the one-electron Hartree-Fock equations depend on their own solutions, they must be solved iteratively, which is known as the self-consistent field method.[44]

Although the Hartree-Fock method provides an exact description of electron exchange, the correlation between the electrons is not fully described.[45] The electronic correlation describes how electrons influence each other beyond the mean-field picture, which is important for an accurate description of the ground state energy. Electronic correlation is, for example, responsible for long range van der Waals interactions and affects also the interaction of overlapping electron densities.[46]

2.2 The density functional theory

An alternative to Hartree-Fock based methods is the Density Functional Theory (DFT). DFT originates from the Thomas-Fermi (TF) model proposed by Thomas[47] and Fermi[48] in 1927. In the TF approach, the energy of electrons is modeled as a functional of the electron density, where the electrons are idealized as non-interacting particles in a homogeneous electron gas. Although the approximation is crude, this was first step towards electronic structure calculations using the electron density as the basic quantity. The theoretical foundation for using the electron density as the basic variable was provided in 1964 by Hohenberg and Kohn with two theorems, which established the density functional theory. The first Hohenberg-Kohn theorem[49] demonstrates the Hamiltonian of the Schrödinger

equation is completely determined by the ground state density and, therefore, all ground state properties of the system are determined by the ground state density. The second Hohenberg-Kohn theorem[49] states the electron density that minimizes the energy of the energy functional is the ground state electron density corresponding to the full solution of the Schrödinger equation. Thus, if the energy functional of a system is known, it is in principle possible to vary the electron density until the energy from the functional is minimized and that electron density is the ground state density.

Although the Hohenberg-Kohn theorems are powerful, it is still difficult to calculate the total energy because the energy functional is unknown. However, thanks to the Kohn-Sham equations, DFT has become a practical tool. The energy functional in the Kohn-Sham approach for a many-body system is given by:

$$E_{\mathrm{KS}} = T_0[n(\mathbf{r})] + \int n(\mathbf{r}) V_{\mathrm{ext}}(\mathbf{r}) d\mathbf{r} + E_{\mathrm{H}}[n(\mathbf{r})] + E_{\mathrm{xc}}[n(\mathbf{r})]. \tag{2.5}$$

The first term is the kinetic energy of non-interacting electrons with density $n(\mathbf{r})$. The second term describes the interaction between the electrons and the atomic nuclei or any other external fields. The third term is the classical electrostatic (Hartree) energy, which describes the Coulomb repulsion energy between an electron and the total electron density defined by all electrons in the system. The final term is an implicit definition of the exchange-correlation energy which contains the non-classical electrostatic interaction energy and the difference between the kinetic energies of the interacting and non-interacting systems. An important part of Kohn-Sham approach is to introduce an exchange-correlation term with quantum mechanical effects as the other terms can, in principle, be calculated exact.[50]

With the Kohn-Sham separation for the energy functional, the one-electron Schrödinger-like equations for the electronic system can be written as

$$(-\frac{1}{2}\nabla^2 + V_{\mathrm{KS}}(\mathbf{r}))\psi_i(\mathbf{r}) = \varepsilon_i \psi_i(\mathbf{r}). \tag{2.6}$$

This is the Kohn-Sham equations.[51] The $\mathrm{V_{KS}}(\mathbf{r})$ is called the Kohn-Sham potential, and is given by

$$V_{\mathrm{KS}}(\mathbf{r}) = V_{\mathrm{ext}}(\mathbf{r}) + V_{\mathrm{H}}(\mathbf{r}) + V_{\mathrm{xc}}(\mathbf{r}). \tag{2.7}$$

The exchange-correlation potential $\mathrm{V_{xc}}(\mathbf{r})$ is

$$V_{\mathrm{xc}}(\mathbf{r}) = \frac{\delta E_{\mathrm{xc}}[n(\mathbf{r})]}{\delta n(\mathbf{r})}. \tag{2.8}$$

By solving Kohn-Sham equations, the electron density in terms of the individual electron wave function can be constructed from

$$n(\mathbf{r}) = 2\sum_{i=1}^{N} \psi_i^*(\mathbf{r})\psi_i(\mathbf{r}). \tag{2.9}$$

Here, the factor of 2 appears as each one electron orbital can be occupied by two separate electrons with different spins. The kinetic energy of non-interacting electrons with density

$n(\mathbf{r})$ is

$$T_0[n(\mathbf{r})] = \sum_{i=1}^{N} \int -\frac{1}{2}\psi_i^*(\mathbf{r})\nabla^2\psi_i(\mathbf{r})d\mathbf{r}. \tag{2.10}$$

As the Kohn-Sham potential $V_{KS}(\mathbf{r})$ depends on the electron density $n(\mathbf{r})$, it is necessary to solve also the Kohn-Sham equations self-consistently.

For the open-shell system, it is needed to split the electron density into two spin densities $\rho_\uparrow(\mathbf{r})$ and $\rho_\downarrow(\mathbf{r})$. The exchange-correlation functional depends in this case on the individual spin densities, while the external and Hartree potentials depends on the full electron density $\rho(\mathbf{r})$.

2.2.1 Exchange-correlation energy – nature's glue

The exchange-correlation energy must be specified to obtain the Kohn-Sham DFT energy. On an absolute scale, the $E_{xc}[n(\mathbf{r})]$ term is generally smaller than the other terms. However, the balance between the kinetic energy $T_0[n(\mathbf{r})]$ and the electrostatic energy (including $\int n(\mathbf{r})V_{ext}(\mathbf{r})d\mathbf{r}$ and $E_H[n(\mathbf{r})]$) may make the exchange-correlation energy the dominant part in total energy differences. Ref. [52] shows an example, where the energy difference between different Cu_8 isomers is determined by the exchange-correlation energy. $E_{xc}[n(\mathbf{r})]$ plays in many cases an important role in the formation of bonds. Thus, $E_{xc}[n(\mathbf{r})]$ can be viewed as the "glue" that binds atoms together.[52]

2.2.2 Approximations to the exchange-correlation energy

One merit of the Kohn-Sham approach is the separation of the energy terms in Equation 2.5, which puts all quantum effects in the exchange-correlation energy term. A first approach to estimate $E_{xc}[n(\mathbf{r})]$ is the local density approximation (LDA),[49;51] where a general inhomogeneous electronic system is considered as locally homogeneous. The exchange and correlation give rise to an exchange-correlation hole around each electron in the homogeneous electron gas. The hole can be attributed to the exclusion radius caused by the Pauli exclusion principle.[53] In LDA, $E_{xc}^{LDA}[n(\mathbf{r})]$ is written as:

$$E_{xc}^{LDA}[n(\mathbf{r})] = \int \varepsilon_{xc}^{hom}[n(\mathbf{r})]n(\mathbf{r})d\mathbf{r}, \tag{2.11}$$

where $\varepsilon_{xc}^{hom}[n(\mathbf{r})]$ is the exchange-correlation energy per electron in a homogeneous electron gas of density $n(\mathbf{r})$. Despite its simplicity, LDA can, *e.g.*, predict trends in formation energies.[54] However, it was early realized that only the local density at each point is not a suitable approximation for the rapidly varying electron densities of many materials, and that the gradient of the density ($\nabla n(\mathbf{r})$) needs to be considered.

A significant improvement in the accuracy of the evaluation of $E_{xc}[n(\mathbf{r})]$ can be obtained by using both $n(\mathbf{r})$ and $\nabla n(\mathbf{r})$, *e.g.*, the generalized gradient approximation (GGA).[55;56] With the modified exchange-correlation functional, the exchange-correlation energy will be:

$$E_{xc}^{GGA}[n(\mathbf{r})] = \int \varepsilon_{xc}^{hom}[n(\mathbf{r})]F_{xc}[n(\mathbf{r}), \nabla n(\mathbf{r})]d\mathbf{r}, \tag{2.12}$$

where $F_{\mathrm{xc}}[n(\mathbf{r}), \nabla n(\mathbf{r})]$ is the enhancement factor. GGA is sometimes referred to as a "semi-local" functional owing to its dependence on $\nabla n(\mathbf{r})$. Perdew and coworkers have proposed a set of GGA functionals, among which PBE[55;56] (Perdew-Burke-Ernzerhof) is widely used.

GGA works generally better than LDA especially in the prediction of bond lengths and binding energies. However, GGA (and also LDA) performs poorly when dealing with strongly correlated system, such as transition metal oxides and rare-earth materials. For example, GGA fails to describe the band gap of Cu_2O.[57] The issue is connected to the unphysical self-interaction error in the Hartree potential term (Equation 2.7) that is not completely accounted for in GGA. In the Hartree-Fock approach, this fictitious self-interaction is corrected by the exchange energy, which motivates the development of functionals that combines these two approaches, *i.e.*, hybrid functionals.[58]

By adding exact exchange energy from the Hartree-Fock approach ($E_{\mathrm{x}}^{\mathrm{HF}}$) to DFT, properties such as bond lengths, binding energies and electronic band gaps can be described with higher accuracy. The linear combination of $E_{\mathrm{x}}^{\mathrm{HF}}$ with a LDA or GGA functional defines a hybrid functional.[59] Generally, the exact $E_{\mathrm{x}}^{\mathrm{HF}}$ and the LDA or GGA exchange energy is scaled, and the full correlation energy from LDA or GGA is used. The exchange-correlation energy will in this way be:

$$E_{\mathrm{xc}}^{hybrid} = \alpha E_{\mathrm{x}}^{\mathrm{HF}} + (1-\alpha) E_{\mathrm{x}}^{\mathrm{DFT}} + E_{\mathrm{c}}^{\mathrm{DFT}}, \tag{2.13}$$

where the coefficient α can, for example, be fitted to properties of a molecular databases.[59] In this thesis, a screened hybrid functional of Heyd, Scuseria, and Ernzerhof (HSE)[60] with 25% short range Hartree-Fock exact exchange, which is called HSE06,[61] is used.

Another possibility to improve the description on the strongly correlated d or f electrons in transition-metal oxide or rare earth elements is to add an additional on-site repulsion term U to the Kohn-Sham Hamiltonian in the, so-called, Hubbard-U approach.[62–64] The added U term can compensate the over delocalization that originates from the self-interaction in LDA and GGA. The effect of the added U term is to stabilize the localized orbitals relative to the other orbitals.[45] The determination of the Hubbard parameter U can be done either empirically by fitting it to bulk values or self-consistently from first principles.[65;66]

LDA, GGA or hybrid functionals do not account for van der Waals interaction. The van der Waals interaction originates from the interaction between fluctuating dipoles. One common approach to account for vdW-interactions is to include a semi-empirical correction to Kohn-Sham DFT as proposed by Grimme and co-workers.[67–70] The dispersive energy in these, so-called, D2/D3 schemes, is described by damped interatomic potentials. For D2, E_{disp} is given by[68]

$$E_{disp} = -s_6 \sum_{i=1}^{N_{at}-1} \sum_{j=i+1}^{N_{at}} \frac{C_6^{ij}}{R_{ij}^6} f_{dmp,6}(R_{ij}) \tag{2.14}$$

N_{at} is the number of atoms in the system, C_6^{ij} is the dispersion coefficient for atom pair ij which can be calculated from atomic polarizabilities. s_6 is a global scaling factor that depends on the applied xc-functional, and R_{ij} is the interatomic distance. In order to

avoid near-singularities for small R and contributions from short-range interactions, a damping function f_{dmp} is used. For the D3 scheme,[69] higher-order dispersion terms C_8 is included, yielding

$$E_{disp} = -s_6 \sum_{i=1}^{N_{at}-1} \sum_{j=i+1}^{N_{at}} \frac{C_6^{ij}}{R_{ij}^6} f_{dmp,6}(R_{ij}) - s_8 \sum_{i=1}^{N_{at}-1} \sum_{j=i+1}^{N_{at}} \frac{C_8^{ij}}{R_{ij}^8} f_{dmp,8}(R_{ij}). \tag{2.15}$$

The dispersion coefficients C_6^{ij} are in D3 computed from first principles and the higher-order dispersion terms C_8 are calculated recursively based on the C_6^{ij} coefficients.

Another approach is to augment LDA and GGA functional with nonlocal correlation energy. In this thesis, Bayesian error estimation functional (BEEF) and nonlocal van der Waals density functional (vdW-cx) are used. BEEF is a semi-empirical density functional developed with Bayesian statistics and experimental data of molecular, surface chemical and solid state materials properties.[71–73] The construction allows for error estimation of the calculated reaction energies.

Nonlocal correlation of the van der Waals density functional by Dion and coworkers[74–78] (vdW-DF) is constructed from first principles. The total exchange-correlation energy in the vdW-DF is given by:

$$E_{\mathrm{xc}} = E_{\mathrm{x}}^{\mathrm{GGA}} + E_{\mathrm{c}}^{\mathrm{LDA}} + E_{\mathrm{c}}^{nl}. \tag{2.16}$$

The first two parts are GGA exchange and LDA correlation. The van der Waals interaction enters through a fully nonlocal correlation term E_c^{nl}. In this thesis, the vdW-cx functional has been used.[78]

2.3 DFT in practice

The Kohn-Sham equations provide the fundamental equations to find the ground state density and ground state energy of a many-body electron problem. To solve the Kohn-Sham equations numerically, the mathematical problem of solving the eigenvalue equation (Equation 2.6) needs to be handled. The problem contains two main issues, 1) the mathematical representation of the one-electron orbitals; 2) the description on electron-nucleus interaction.

2.3.1 Plane wave basis set

Thanks to Bloch's theorem, the properties of the electrons within a periodic structure can be calculated by solving the Kohn-Sham equations in the unit cell.[79] Bloch's theorem states that the wave function of an electron in an external periodic potential with the unit vector $\mathbf{a}_i$ can be expressed by the product of a function with the same periodicity of the potential, *i.e.*

$$\psi_{\mathbf{k}}(\mathbf{r}) = e^{i\mathbf{k}\cdot\mathbf{r}} u_{\mathbf{k}}(\mathbf{r}), \tag{2.17}$$

where $e^{i\mathbf{k}\cdot\mathbf{r}}$ are plane waves and $u_{\mathbf{k}}(\mathbf{r}) = u_{\mathbf{k}}(\mathbf{r} + \mathbf{a}_i)$. The $\mathbf{r}$ vectors are represented in real space whereas $\mathbf{k}$ are given in reciprocal space. Bloch's theorem also means that it is possible to solve the Kohn-Sham equations for each $\mathbf{k}$ independently, where the electronic

wave functions at each **k** value can be expanded in terms of a discrete plane-wave basis set.[79] It turns out that solving the integral over **k** values in reciprocal space is more convenient than over **r** in real space.[79]

2.3.2 Pseudopotentials

The use of plane waves require that the wave function is smooth, which it is in the chemical bonding area. However, the wave functions have wiggles near the nuclei and it is difficult to describe those fast variations using a plane wave basis set.[45] Chemically, the core electrons are not particularly important in forming the bonds. Therefore, pseudopotentials have been developed to replace the electron density from the core electrons with a smoothed density, which dramatically decrease the number of the plane waves in the calculations.[80;81] In this approach, the core electrons are considered to be frozen. There are several forms of pseudopotentials used in plane-wave based DFT codes. In this thesis, the projector augmented wave method (PAW)[80] is used. One advantage with the PAW method is that the approach keeps the entire set of all-electron core wave functions and the smooth parts of the valence wave functions.

2.3.3 Solving the Kohn-Sham equations

The Kohn-Sham equations (Equation 2.6) need to be solved self consistently. Practically, it starts with an input electron density and the output electron density is calculated by the electron wave function through Equation 2.9, where this electron wave functions are constructed by solving the Kohn-Sham eigenvalue problem. The self-consistent loop will be terminated if the input electron density equals the output electron density within a certain numerical tolerance. Given that the total energy and the electron density are unambiguous one-to-one mapped with each other,[49] the self-consistency condition can also be complied with the variation of the total energy within a certain numerical tolerance. During the procedure, the new input electron density for the next iteration will be constructed by mixing and extrapolating from the previous electron density to continue the next iterations until it reaches the criteria.[45]

Chapter 3

Calculations of measurable properties

> ***The transitory nature of some of the intermediates implicated in catalysis are such that their structures can best be ascertained by computational procedures, rather than by direct, experimental ones.***
>
> — John Meurig Thomas & W. John Thomas[82]

Catalysts are experimentally characterized in different ways. The activity and selectivity can be obtained by measuring the rate of the formation of the products. Probing the activity as a function of the temperature gives information on the apparent activation energy and preexponential factor via the Arrhenius equation. Measuring the activity as a function of reactant pressures yields information on the reaction orders. This kind of kinetic characterization can be coupled to atomic scale calculations by micro-kinetic modeling where the parameters of the elementary steps have been obtained from first principles (FP).[83]

The success of a FP-based kinetic model is dependent on the relevance of the atomic scale model of the catalyst, thus the composition and the structure. This kind of information is experimentally obtained by physical characterization. The experimental characterization is generally not direct, and calculations may be needed to interpret the results. Hence, FP-calculations could be useful also for this type of characterization.

Figure 3.1 sketches different types of information that commonly are obtained from experimental characterization. By doing activity tests, information on the reaction kinetics, such as apparent activation energies and reaction orders can be obtained. By use of temperature-programmed desorption or reaction (TPD or TPR) techniques, it is possible to characterize the adsorption and reaction energies. By use of infrared (IR) spectroscopy, the vibrational frequencies of gas phase and surface species can be obtained. Surface species can in this way be determined by comparing the vibrational signatures with reference spectra. While interaction with infrared light causes surface species to undergo vibrational transitions, higher energy radiation in the UV and visible range of the electromagnetic spectrum can induce excitation of valence electrons, which gives information about the electronic structure in the valence region. With radiation in X-ray range of the electromagnetic spectrum, the core-level binding energies can be monitored and give information on the chemical state of the catalyst.

The information on surface species and catalysts can also be obtained by FP calculations. The atomic structure can be obtained by doing geometry optimization. The state of the catalysts during the operando conditions can be obtained by *ab initio* thermodynamics. The vibrational frequencies of a species can be calculated either by finite differences approach or by molecular dynamics. The electronic structural analysis, *i.e.*, density of

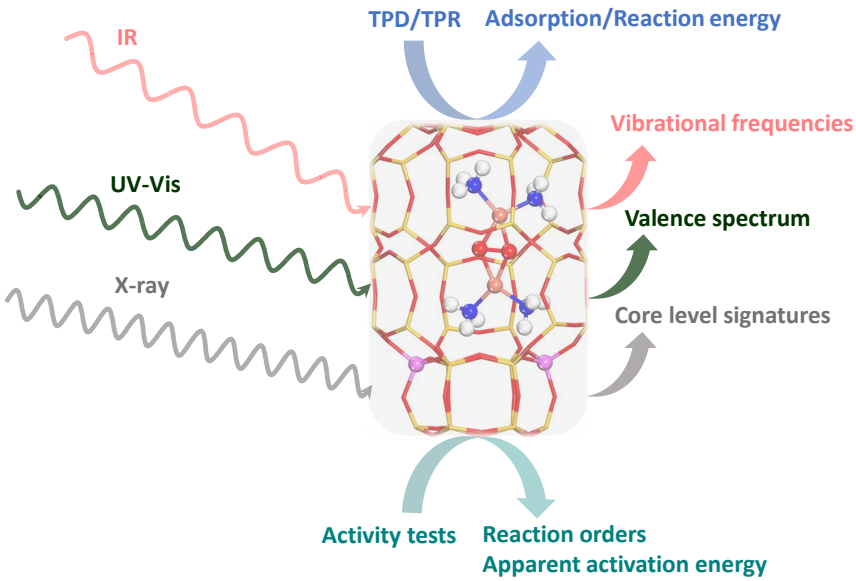

Figure 3.1: Sketch of typical information obtained from experimental studies of catalytic reactions. The structure in the center of this picture is an activated oxygen over the oxidized Cu complex pair in the CHA cage.

states and charge analysis, give information on bond character and oxidation states. The energetic reaction barriers can be calculated by the transition state searches and the free energy barriers can be calculated via partition functions by vibrational analysis or by explicit constrained molecular dynamics. By combining the FP calculations with kinetic simulation, TPD profiles can be simulated. This chapter discusses how different measurable properties can be calculated.

3.1 Atomic structure

The arrangement of the atoms is in electronic structure calculations obtained by geometry optimization. The process in a geometry optimization is to minimize the total energy of a set of atoms, $E(\mathbf{x})$, by varying the positions of the atoms. Minimizing $E(\mathbf{x})$ is equivalent to finding a stationary point, where the first derivative $(\partial E(\mathbf{x})/\partial x_i)$ is zero and all the second derivative $(\partial^2 E(\mathbf{x})/(\partial x_i \partial x_j))$ are positive for $i, j = 1,...,3N$, where N is the number of atoms.

In the common optimization methods, the gradient $\mathbf{g}$, *i.e.* the first derivative of the energy with respect to all variables, is calculated numerically. The gradient vector $\mathbf{g}$ points in the direction where the function increases most. In the Steepest Descent (SD) method, a series of steps are performed following the gradient of the previous step along the search direction.[84] Although the SD method is robust, it often converges slowly near the minima as the history gradient is not kept. In this thesis, the conjugate-gradient (CG)[85] method implemented in VASP[86;87] is used to minimize the total energy and to

obtain optimized structures. Unlike the SD method, the CG method makes use of the gradient history and every new search direction is a conjugate direction to the previous step.

These optimization methods basically find the nearest stationary point, however, many stationary points may exist on a complicated PES. The minimum with the lowest energy value is the global minimum and the others are local minima. For some cases, it is important to sample a large set of these local minima, which is called conformational sampling. Generally, there are two main approaches to do the conformational sampling, Monte Carlo and molecular dynamics simulation. In this thesis, *ab initio* molecular dynamics is performed to search for the low-energy configurations, which is discussed below.

3.2 Vibrational frequencies

Atoms in molecules and solids vibrate at 0 K via the zero-point motion. The molecular vibrations are given by the normal modes and each normal mode is in this thesis described as a harmonic oscillator in the classic treatment of molecular vibrations. This can be achieved by expanding the energy as a function of the nuclei coordinates in a Taylor expansion around the equilibrium position.[79] For a diatomic molecule, the energy is described by the bond length r:

$$E(r) = E(r_0) + \frac{dE}{dr}(r - r_0) + \frac{1}{2}\frac{d^2E}{dr^2}(r - r_0)^2 + \frac{1}{6}\frac{d^3E}{dr^3}(r - r_0)^3 + \cdots, \tag{3.1}$$

where r_0 is the bond length at the equilibrium state. The first term is the ground state energy of the system. The second term is zero because it is evaluated at the energy minimum where the derivative is zero. Thus, the energy is in the harmonic approximation:

$$E(r) = E(r_0) + \frac{1}{2}\frac{d^2E}{dr^2}(r - r_0)^2. \tag{3.2}$$

The higher order terms are anharmonic corrections to the vibration. They are typically only a few percent of the energy. In an N-atom system, there will be 3N degrees of freedom [$\mathbf{r} = (r_1, r_2, \cdots, r_{3\mathrm{N}})$]. If $\mathbf{r_0}$ is a local minima in the energy of the system, the Taylor expansion for the energy of the system around the minimum at $\mathbf{r_0}$ can be written:

$$E(\mathbf{x}) = E(r_0) + \frac{1}{2}\sum_{i=1}^{3N}\sum_{j=1}^{3N}\frac{\partial^2 E}{\partial x_i \partial x_j}x_i x_j, \tag{3.3}$$

where $\mathbf{x} = \mathbf{r}$ - $\mathbf{r_0}$. There are 3N $\times$ 3N possible second derivatives and the matrix of these second derivatives is called the Hessian matrix, which is:

$$H(ij) = \frac{\partial^2 E}{\partial x_i \partial x_j}. \tag{3.4}$$

Treating the atoms as classic particles following Newton's and Hooke's laws, the equation of the motion can be written as

$$\frac{d^2\mathbf{x}}{dt^2} = -\mathbf{A}\mathbf{x}. \tag{3.5}$$

Here, $\mathbf{A}$ is the mass-weighted Hessian matrix with $A_{ij} = H_{ij}/m_i$. The eigenvectors $\mathbf{e}$ of this matrix and the corresponding eigenvalues λ are determined by $\mathbf{Ae} = \lambda\mathbf{e}$. Therefore, to obtain the normal modes from FP calculations, the main task is to calculate the elements of Hessian matrix $\mathbf{H}_{ij}$. By using the finite-difference approximation, the Hessian matrix can be estimated by

$$H_{ij} = \frac{\partial^2 E}{\partial x_i \partial x_j} \approx \frac{(E(\delta x_i, \delta x_j) - E_0) - (E_0 - E(-\delta x_i, -\delta x_j))}{\delta x_i \delta x_j}. \tag{3.6}$$

$\mathbf{A}$ is defined once all the elements of the Hessian matrix $\mathbf{H}$ are calculated. Thereby, the 3N normal mode frequencies are given by the 3N eigenvalues of the mass-weighted Hessian matrix $\mathbf{A}$. The atomic motions, which correspond to a normal mode frequency, are determined by the eigenvector of $\mathbf{A}$. Each normal mode frequency ν_i is then given from the eigenvalue λ_i via $\nu_i = \sqrt{\lambda_i}/2\pi$.

3.3 State of the catalysts

The ground state properties obtained from DFT calculations are calculated at zero-temperature and zero-pressure conditions. However, most experiments are performed at elevated temperatures and pressures. Thermodynamics and statistical mechanics can be used in combination with DFT to link the microscopic regime to the macroscopic regime[88;89] by *ab initio* thermodynamics. To estimate the thermodynamic variables in a statistical ensemble, partition functions are used to calculate free energies.[90] The partition function for a system is defined as:

$$q = \sum_{i}^{\infty} e^{-\beta\varepsilon_i} \tag{3.7}$$

where β is $1/(k_B T)$ and ε_i is the total energy corresponding to the state i. For N non-interacting particles (ideal gas), the total partition function Q is q^N for the case where the particles are independent and distinguishable. The partition function is $q^N/N!$ if the particles are independent and indistinguishable. For N interacting particles like liquid or solid state, the partition function Q is obtained by summing over all energy states E_i for the entire system and is given by $Q = \sum_i^{\infty} e^{-\beta E_i}$. As the energy levels for interacting system is continuous, the sum can be replaced by an integral. The thermodynamic state functions, such as the internal energy U, Helmholtz free energy A, pressure P, enthalpy

H, entropy S and Gibbs free energy G can be derived from the partition function:[84]

$$\begin{aligned} U &= k_B T^2 (\frac{\partial lnQ}{\partial T})_V \\ A &= U - TS = -k_B T lnQ \\ P &= -(\frac{\partial A}{\partial V})_T = k_B T (\frac{\partial lnQ}{\partial T})_T \\ H &= U + PV = k_B T^2 (\frac{\partial lnQ}{\partial T})_V + k_B TV (\frac{\partial lnQ}{\partial T})_T \\ S &= \frac{U - A}{T} = k_B T (\frac{\partial lnQ}{\partial T})_V + k_B lnQ \\ G &= H - TS = k_B TV (\frac{\partial lnQ}{\partial T})_T - k_B T lnQ \end{aligned} \tag{3.8}$$

For an isolated molecule, the total energy is the sum of translational, rotational, vibrational and electronic energy. This implies the partition function can be written as a product of these degrees of freedom:

$$\begin{aligned} q_{tot} &= q_{trans}\, q_{rot}\, q_{vib}\, q_{elec} \\ H_{tot} &= H_{trans} + H_{rot} + H_{vib} + H_{elec} \\ S_{tot} &= S_{trans} + S_{rot} + S_{vib} + S_{elec}. \end{aligned} \tag{3.9}$$

The transitional partition function of a molecule confined in a volume V is:[91]

$$q_{trans} = \frac{(2\pi M k_B T)^{3/2}}{h^3} V \tag{3.10}$$

where M is the mass of the molecule. V can be related to the pressure via the ideal gas law. Within the rigid-rotor approximation, the rotational partition function for a non-linear molecule is given by:

$$q_{rot} = \frac{\sqrt{\pi}}{\sigma} (\frac{8\pi^2 k_B T}{h^2})^{3/2} \sqrt{I_1 I_2 I_3} \tag{3.11}$$

where σ is the symmetry index of the molecule and I_x(x=1,2,3) is the moments of inertia along three spatial axes. For a diatomic molecule with only two degrees of freedom to rotate, the partition function is:

$$q_{rot} = \frac{8\pi^2 k_B T I}{\sigma h^2}. \tag{3.12}$$

The vibrational partition function for a molecule is given as:

$$q_{vib} = \prod_i \frac{e^{-hv_i/2k_B T}}{1 - e^{-hv_i/k_B T}} \tag{3.13}$$

where v_i is the vibration frequency of mode i.

The electronic partition function is a sum over all electronic quantum states. However, the energy difference between the ground and excited states is usually much larger than $k_B T$.[84] Thus, the electronic partition function is:

$$q_{elec} \approx e^{-E_0/k_B T}. \tag{3.14}$$

With the above partition functions, the enthalpy and entropy terms can be calculated using equation 3.8. Therefore, for a specific system with a single conformation, the Gibbs free energy from a DFT calculations can be derived as

$$G = E_{elec} + \Delta G_{trans} + \Delta G_{rot} + \Delta G_{vib} + \Delta G_{elec}. \tag{3.15}$$

With the calculated Gibbs free energies, phase diagrams can be constructed to determine the state of the catalysts under a certain experimental condition. For example, given chemical equilibria between adsorbed and gas-phase species, it is possible to construct a pressure-temperature phase diagram by minimizing the total Gibbs free energy.

3.4 Analysis of the electronic structure

To know the physical properties of a catalyst, the ground state properties of the electrons must be calculated. In this thesis, the electronic structure is analyzed by calculating the density of states. The charge distribution is analyzed by calculating the Bader charges.

3.4.1 Density of states

The electronic density of states (DOS) defines the number of electronic energy states lying between the energy interval E and $E + dE$. Once a DFT calculation is performed, the DOS for the given energy E, is defined by[45]

$$\rho(E) = \frac{1}{N_k} \sum_{i,k} \delta(\varepsilon_{i,k} - E). \tag{3.16}$$

where $\varepsilon_{i,k}$ denotes the Kohn-Sham energy of an electron. Thus the electronic density of states represents the Kohn-Sham energy spectra. By projecting the Kohn-Sham eigenstates onto an atomic basis, the relative contribution from a particular orbital to the total DOS can be obtained, which is called project density of states (PDOS).

3.4.2 Bader charge analysis

It is of interests to analyze the charge transfer between the ions during a reaction as the charge transfer gives information on the change of the oxidation state and charge localization. Bader charge analysis[92] is one common method that is applicable within plane-wave DFT calculations. Bader decomposition uses stationary points in the electron density $\rho(x, y, z)$ to partition electrons among different atoms. The stationary point is defined as no flux in the gradient vector field of $\rho(x, y, z)$ in the electron density surface.

Thus, separation of the electrons between atoms is determined by "zero-flux" boundary condition:[93]

$$\nabla\rho(\mathbf{r}) \cdot \mathbf{n}(\mathbf{r}) = 0, \tag{3.17}$$

where $\mathbf{n(r)}$ is a unit vector normal to the surface at $\mathbf{r}$. At a point on a dividing surface, the gradient of the electron density has no component normal to the surface. In this thesis, a grid-based approach developed by Henkelman and co-workers[94] has been used for partitioning the charge density. In this approach, the partitioning algorithm follows the steepest ascent paths along the charge density gradient from grid point to grid point until a charge density maximum is reached.

3.5 Reaction barriers

Empirically, the Arrhenius equation $k(T) = \nu exp(-E_a/k_BT)$ describes the dependence of the reaction rate constant k on the absolute temperature T, where ν is the preexponential factor and E_a is the activation energy. As the activation energy is the energy difference between the energy minimum and the transition state, the transition state needs to be determined to obtain the E_a.

3.5.1 Transition state search

Although recent experiments have probed the transition state for CO reacting with atomic O on a ruthenium surface,[95] it is generally not possible to directly detect the transitory character of a chemical transformation by experimental tools. As an alternative, the advances of first principle calculations have allowed for atomic scale descriptions of the transition state for a reaction.

On a specific PES, the transition state (TS) connects two adjacent minima (for the reactant and the product). The TS is a point on the PES that is a minimum in all directions but one, which implies that one of the vibrational frequency at the TS is imaginary. One widely used method for finding the TS is the *nudged elastic band* (NEB) method.[96;97] This method is based on the interpolation between two minima, which are corresponding to the reactant and product structures. The interpolation method assumes that the TS state is located somewhere between the two minima.

The NEB is a chain-of-states method with a string of images (geometry configurations), which represents the reaction path. The images are connected by spring forces as "nudging" by a spring constant k which will be distributed evenly along the path. The images along the NEB should be converged to the minimal energy path (MEP). An illustration of this method is shown in Figure 3.2. The relaxation of NEB to the MEP is performed by a force projection scheme and the NEB force on image i is projected by

$$F_i^{\mathrm{NEB}} = F_i^{\perp} + F_i^{\mathrm{SII}}, \tag{3.18}$$

where $F_i^{\perp}$ is the component of the force perpendicular to elastic band and F_i^{SII} is the spring force parallel to the band. The tangent $\hat{\tau}_i$ along the band is the unit vector to the neighboring image with higher energy. During the constrained relaxation, the spring force will not interfere with the relaxation of the images perpendicular to the path and

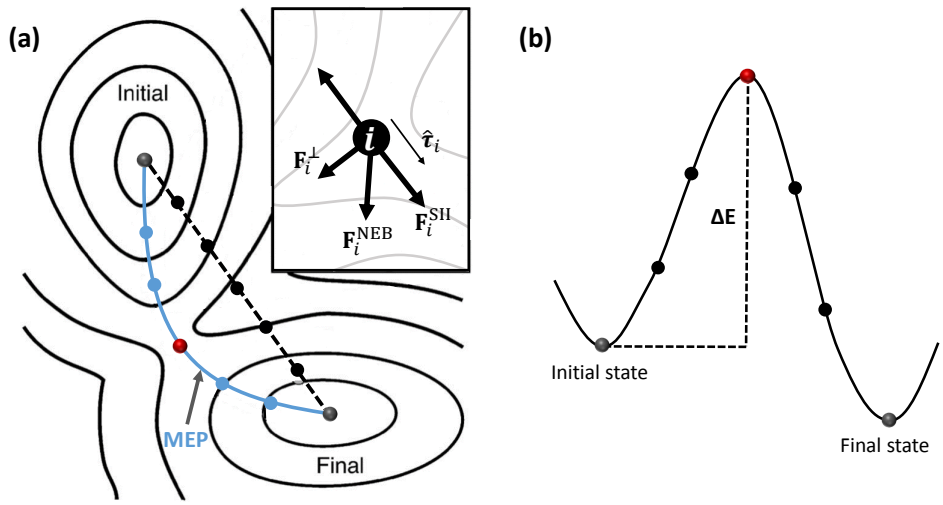

Figure 3.2: (a) Schematic picture of the nudged elastic band (NEB) method. The blue line is the minimum energy path with 5 intermediate images. (b) The potential energy profile along the minimum energy path. This figure is adapted from Ref. [97].

it will converge when the total force $F_i^{\perp}$ is within a defined criteria. To find the saddle point, MEP can be further optimized by the climbing-image NEB (CI-NEB).[98] During the CI-NEB, the spring forces on the highest energy image will be removed and the component of the potential force parallel to the chain is reversed, which enable it move towards the saddle point. If the CI-NEB calculation converges, the climbing image will converge to the saddle point.

3.5.2 Thermodynamic integration of free-energy gradients

The free energy barrier of a reaction has one enthalpy part and one entropy part. The enthalpy part can be computed by the NEB method, whereas the entropy part can be calculated via the partition functions. An alternative way to calculate the free energy difference along the reaction path is by thermodynamic integration[99]. This approach uses constrained *ab initio* molecular dynamics.

The term *ab initio* molecular dynamics refers to molecular dynamics simulations based on a PES from FP by using a quantum mechanical method, such as DFT. By calculating the PES on the fly, the forces on the nuclei can be calculated. The motion of the nuclei is calculated by solving Newton's equations of motions:

$$M_i \frac{dv_i}{dt} = -\frac{\partial E}{\partial R_i} \tag{3.19}$$

where v_i is the velocity of the nuclei, M_i is the corresponding nuclei mass, R_i is the nuclei coordinates and E is total potential energy.

In this thesis, the molecular dynamics simulation are performed using the so-called Born-Oppenheimer Molecular Dynamics (BOMD).[100] The potential energy is in BOMD minimized in every MD step. There is another kind of *ab initio* molecular dynamics, called Car-Parrinello MD.[101] As opposed to BOMD, Car-Parrinello MD simulations treat the parameters describing the electronic wave functions as classical degrees of freedom and propagate them as such, instead of solving directly for the wave function at each time step.

During the molecular dynamics, the equation of motion are integrated numerically by use of the Verlet algorithm:[102]

$$R_i(t + \Delta t) \approx 2R_i(t) - R_i(t - \Delta t) + \frac{dv_i(t)}{dt}\Delta t^2. \tag{3.20}$$

Without temperature control, a molecular dynamics simulation behaves as a micro-canonical ensemble (constant N, V, E). However, under typical experimental condition, the system is able to exchange heat with the environment. To compare the MD results with experimental observations, we would like to use the canonical ensemble with constant N, V, T. To simulate a canonical ensemble, a thermostat method is needed to control the temperature. The temperature of the system is given by the equipartition theorem:

$$\sum_i \frac{1}{2} M_i v_i^2 = \frac{3}{2} N k_B T \tag{3.21}$$

where T is the instantaneous temperature and N is the number of atoms. One simple way to simulate the canonical ensemble was proposed by Nosé[103;104] by introducing an extended Lagrangian with an extra degree freedom of heat bath, s,:

$$L = \frac{1}{2}\sum_i M_i s^2 v_i^2 - E + \frac{Q}{2}(\frac{ds}{dt})^2 - g k_B T ln(s) \tag{3.22}$$

where Q is an imaginary mass and g is the number of independent momentum degrees of freedom of the nuclei in the system. Hoover[105] has further improved the extended Lagrangian by introducing a friction coefficient ξ:

$$\begin{aligned} \frac{dv_i}{dt} &= -\frac{1}{M_i}\frac{\partial E}{\partial R_i} - \frac{\xi}{M_i} v_i \\ \xi &= \frac{dln(s)}{dt} \end{aligned} \tag{3.23}$$

With this ξ, the MD simulation temperature will be controlled through:

$$\frac{d\xi}{dt} = \frac{3Nk_B}{Q}(T - T_{Target}). \tag{3.24}$$

Thus, if the instantaneous temperature is too high, ξ will be smoothly adjusted by equation 3.24 and will directly effect the velocities of the nuclei, which will correspondingly reduce the kinetic energy of the system. This approach to control the temperature is known as a Nosé-Hoover thermostat.

The reversible work of changing a system between two states is an important quantity in statistical mechanics. To calculate the free energy difference A, an integration over a variable ξ of the Hamiltonian is performed:[99]

$$\Delta A_{1\to 2} = \int_{\xi(1)}^{\xi(2)} \left(\frac{\partial A}{\partial \xi}\right)_{\xi^*} \cdot d\xi \tag{3.25}$$

where the negative of the integrand is the mean force and ξ^* is the reaction coordinate. The difference in free energy A between two states corresponds to the work, provided that the work is independent of the path followed in space of the thermodynamic state variables.[106]

Along a desired reaction path, the particular value of the reaction coordinate ξ is of low probability during a normal MD simulation. To overcome this problem, a so-called blue-moon ensemble sampling method can be used.[107] In this method, a constrained trajectory with the reaction coordinate is fixed at a specific value. During this constrained MD, the mean force can be estimated directly from the extended Lagrangian.

3.6 Temperature-programmed desorption profiles

Temperature-programmed desorption (TPD) is widely used for characterization of heterogeneous catalysts. The method is straightforward and based on the measurement of the desorption profile of a pre-adsorbed probe molecule during controlled heating. For zeolites and oxide surfaces, NH_3-TPD is generally used to measure the amount of acid sites together with the acid strength.[108;109] In this thesis, NH_3-TPD profiles from Cu-exchanged zeolites have been simulated to study the interaction between NH_3 and the active site.

The NH_3 desorption profiles have been analyzed following Ref. [111;112] taking readsorption into account. Consequently, the simulated process is:

$$NH_3^* \underset{k_a}{\overset{k_d}{\longleftrightarrow}} NH_3(g) + * \tag{3.26}$$

where $*$ denotes an adsorption site and NH_3(g) is ammonia in the gas phase. k_d and k_a are the desorption and adsorption rate constants, respectively. In the mean-field assumption, the time derivative of the NH_3 coverage (θ) is given by:

$$\frac{d\theta}{dt} = k_a \frac{P_g}{P^0}(1-\theta) - k_d\theta \tag{3.27}$$

where P_g is the pressure of ammonia and P^0 is the pressure at standard conditions. Using the ideal gas law, P_g can be written as RTC_g where R is the gas constant, T is the temperature and C_g is the ammonia concentration. The concentration can be calculated assuming equilibrium between the gaseous and adsorbed ammonia:

$$C_g = \frac{\theta}{1-\theta}\frac{P^0}{RT}K \tag{3.28}$$

where K is the equilibrium constant given by the enthalpy and entropy changes (ΔH and ΔS) upon desorption:

$$K = \frac{k_d}{k_a} = exp(-\frac{\Delta H}{RT})exp(\frac{\Delta S}{R}) \tag{3.29}$$

The mass balance in the flowing gas is:

$$FC_g = -A_0 W \frac{d\theta}{dt} = -\beta A_0 W \frac{d\theta}{dT} \tag{3.30}$$

where F is the flow rate of the carrier gas, A_0 is the concentration of the adsorption sites, W is the zeolite weight and β is the heating rate ($\Delta T = \beta \delta t$). The concentration can in this way be written:

$$C_g = -\frac{\beta A_0 W}{F} \frac{d\theta}{dT} = \frac{\theta}{1-\theta} \frac{P^0}{RT} exp(-\frac{\Delta H}{RT})exp(\frac{\Delta S}{R}) \tag{3.31}$$

The concentration depends on temperature and site-coverage. The site-coverage is obtained iteratively through:

$$\theta_{i+1} = \theta_i + \left(\frac{d\theta}{dT}\right)_i \Delta T \tag{3.32}$$

This relation connects C_g and T, which gives the TPD profile.

Chapter 4

State of Cu-sites during NH_3-SCR

4.1 Introduction

The first step in exploring the mechanism for the NH_3-SCR reaction over Cu-CHA is to investigate the nature of the Cu ions under typical reaction conditions (gas pressures and temperatures). During recent years, it has been found that Cu sites respond sensitively to the operating conditions and that Cu species are solvated by NH_3 under conditions for NH_3-SCR below 250 °C.[36–39;110;111] Cu K-edge XANES spectroscopy in combination with DFT calculations suggest that Cu(I) is present as diamine complexes, $Cu(NH_3)_2^+$.[36–39;110] This linear $Cu(NH_3)_2^+$ complex has high mobility at low temperatures, which, for example, is demonstrated by *ab initio* molecular dynamics.[38] When the temperature increases above 300 °C, the NH_3 ligands will desorb from the $Cu(NH_3)_2^+$ complex giving rise to immobilized Cu(I) bound directly to the zeolite framework.[36–39;110]

The dynamic character of the Cu ions is not only important for the NH_3-SCR reaction, but also for the functionalization of zeolites via solid-state ion-exchange (SSIE). In this chapter, the mechanism for SSIE of Cu(I) in chabazite is discussed. The state of Cu(I) under a range of NH_3 pressures with varying temperatures is also studied by constructing a temperature-pressure phase diagram. Moreover, the interactions between Cu ions and NH_3 is investigated by simulating ammonia temperature-programmed desorption profiles over Cu-CHA.

4.2 Dynamic character of Cu ions in zeolites

4.2.1 Mechanism for solid-state ion-exchange of Cu(I)

Ion-exchanged zeolites are traditionally synthesized via an aqueous route where metal complexes are dissolved in water and mixed with the zeolite in powder form. This procedure has several drawbacks as it is time-consuming and may require consecutive wash-and-dry steps to achieve the desired ion-exchange level.[112] Additionally, ion-exchange into small-pore zeolites, including chabazite may be hindered by bulky aqueous complexes[16] which cannot enter the zeolite cages. An alternative route for ion-exchange of zeolites is the, so-called, solid-state ion-exchange (SSIE) method.[113;114] Traditionally, the SSIE method has been used with high temperatures where a metal salt or oxide are mixed with zeolite powder and heated to 700-800 °C. Metal ions are formed during the heating and diffuse into the zeolite structure.[115;116] Interestingly, it was recently demonstrated that copper could be exchanged into CHA at low temperatures in the presence of ammonia.[117] In particular, facile exchange could be performed at 450 °C. The SSIE method is straightforward and offers an easy way to control the metal loading in the zeolite.

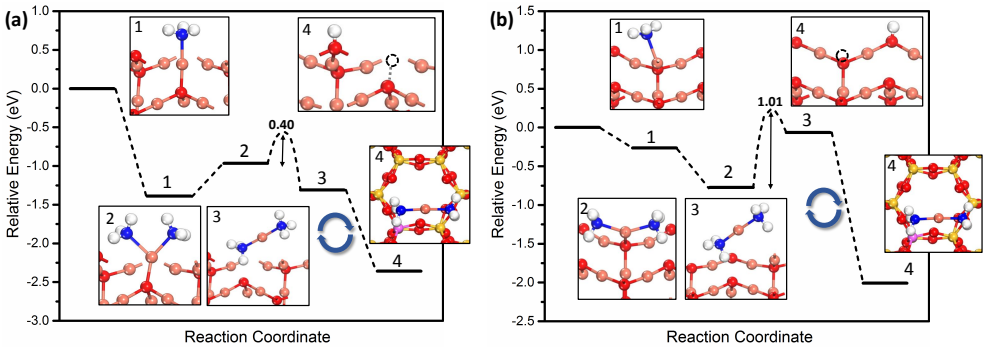

Figure 4.1: Zero-point corrected energies obtained with the HSE06 functional for the SSIE process over the two cuprous oxide surfaces with the $p(1x2)$ surface cell of $Cu_2O(111)$. (a) stoichiometric $Cu_2O(111)$ surface and (b) $Cu_2O(111)$ surface with two Cu_{cus} vacancies. The ion-exchange energy is calculated by comparison of the relative energy of state 3 and step 4. The copper diamine is formed on $Cu_2O(111)$ between state 2 and 3. The copper diamine is located in CHA in state 4 while the proton forms an OH-group on $Cu_2O(111)$.

It has on the basis of Cu K-edge XANES spectra been suggested[39] that Cu^+ diffuses in the form of a diamine complex $Cu(NH_3)_2{}^+$ during the SSIE process. Importantly, the structure and function of copper-exchanged CHA appear to be the same for samples prepared either via the aqueous or SSIE method.[39;117] To explore the mechanisms involved in the SSIE process, a model involving Cu_2O and CHA was proposed in **Paper I**.

Ammonia adsorption is explored on $Cu_2O(111)$ as this is the cuprous oxide surface with the lowest surface energy.[118] Two kinds of $Cu_2O(111)$ surfaces are considered, *i.e.*, the non-polar stoichiometric $Cu_2O(111)$ (denoted as (111)(1×2)) and the unstoichiometric $Cu_2O(111)$ with two Cu vacancies (denoted as (111)(1×2)-V). Sequential ammonia adsorption and $Cu(NH_3)_2{}^+$ formation on the two types of $Cu_2O(111)$ surfaces are shown in Figure 4.1. The first NH_3 is adsorbed on (111)(1×2) by -1.39 eV and the adsorption energy of the second NH_3 is endothermic by 0.42 eV. The adsorption energies have a coverage dependence and the endothermicity is reduced if a large cell is used. Formation of the $Cu(NH_3)_2{}^+$ complex is exothermic compared with the situation of two adsorbed ammonia molecules, with a slight barrier of 0.40 eV. The complex is close to linear with N-Cu distances of about 1.90 Å. The first ammonia adsorbs weaker on the (111)(1×2)-V, with an adsorption energy of -0.26 eV and the adsorption of a second ammonia is clearly exothermic with the formation of a structure where the N-Cu-N axis is parallel to the surface in Figure 4.1(b). The complex is in this case formed with a barrier of 1.01 eV and the adsorbed complex is slightly endothermic with respect to the two adsorbed ammonia molecules. During the exchange step (step from 3 to 4 in Figure 4.1), the complex is moved to the zeolite and the proton is moved to the cuprous oxide surface forming an OH-group. The SSIE processes are in both cases exothermic by -1.05 eV for (111)(1×2) and -1.94 eV (111)(1×2)-V. The considerably higher energy gain for the surface with

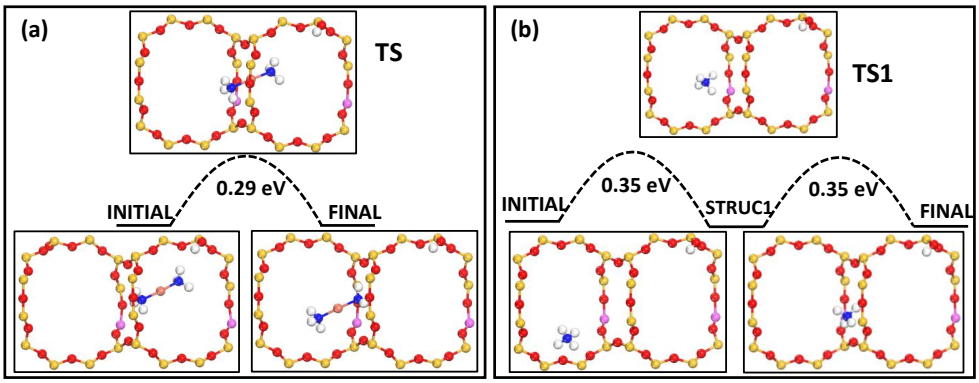

Figure 4.2: Diffusion barrier for (a) diffusion of $Cu(NH_3)_2^+$ through an eight-membered ring and (b) ammonium diffusion through the eight-membered ring in CHA.

vacancies is rationalized by a stronger O-H bond on this surface. The exchange of the H^+ from the zeolite to the oxide surface retains a surface where the proton takes the role of Cu^+. The exchange process is further stabilized by the formation of gas phase water. It is also found that ammonium (NH_4^+) is formed without any barrier when NH_3 is allowed to structurally relax close to a proton in CHA. Therefore, ammonium is assumed to be the proton carrier during the SSIE process.

Knowing that the SSIE exchange process is facile in the presence of ammonia, it becomes important to investigate possible diffusion limitations both for the complex and the ammonium in CHA. The diffusion barrier for the complex $Cu(NH_3)_2^+$ passing through the eight-membered ring is shown in Figure 4.2(a). The insets show the initial, final and transition states. The transition state calculation shows that the diffusion barrier for the complex passing through the eight-member ring is only 0.29 eV. The transition state is with the Cu-ion roughly in the plane of the zeolite ring. Also the diffusion of NH_4^+ in CHA proceeds with low barriers. The diffusion is in this case characterized by three different steps. Ammonium is initially adsorbed in the eight-membered ring, coordinated via a hydrogen bond to an oxygen atom adjacent to Al^{3+} in a four-membered ring. In the first step, ammonium is moved from one eight-membered ring to the neighboring eight-membered ring with a barrier of 0.35 eV. Diffusion through the eight-membered ring has a similar barrier. So has the third step, where ammonium again diffuses between two eight-membered rings. These results show that ammonium easily can facilitate proton transport in the zeolites.

4.2.2 State of Cu^+ during typical reaction conditions

The $Cu(NH_3)_2^+$ complex is found to form without barriers upon NH_3 adsorption on a framework-bound Cu(I) ion in CHA. The two NH_3 ligands are strongly bonded with the Cu(I) ion. Two more NH_3 molecules can also adsorb forming $Cu(NH_3)_3^+$ and $Cu(NH_3)_4^+$

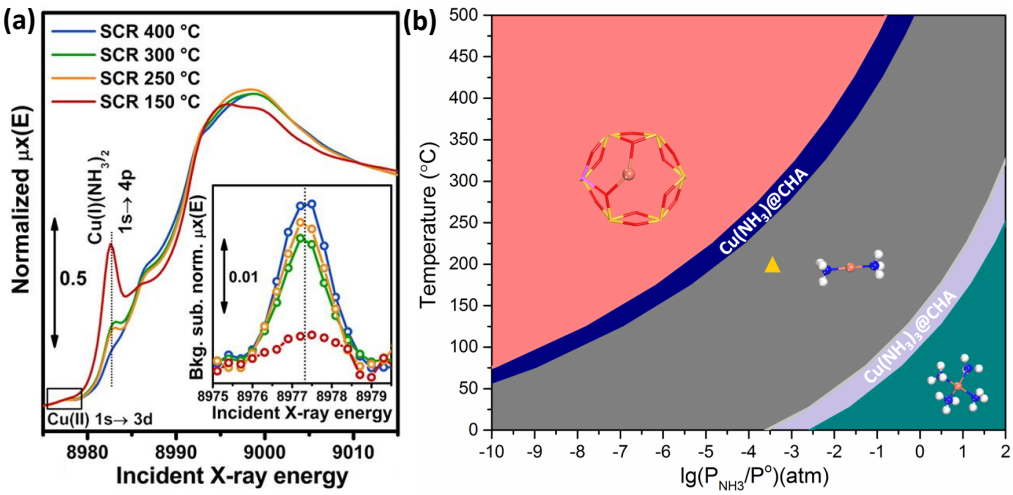

Figure 4.3: (a) Operando XANES spectra during NH_3-SCR at 150, 250, 300 and 400 °C. (b) Phase diagram for $Cu(NH_3)_x^+$ in CHA with varying NH_3 pressure and temperature constructed from DFT. The yellow triangle indicates typical operating conditions, which corresponds to a temperature of 200 °C and an NH_3 concentration of 300 ppm. Atom color codes: copper (pink), aluminum (purple), nitrogen (blue), silicon (yellow), oxygen (red) and hydrogen (white). Figure (a) is reprinted with permissions from Ref. [113]. Copyright (2016) American Chemical Society.

complexes. However, the adsorption energies for the third and fourth NH_3 ligands are $\sim$ 1 eV lower than the first and second NH_3 ligands. To study the thermodynamic stability of the $Cu(NH_3)_2{}^+$ complex with respect to NH_3 partial pressure and temperature, a temperature-pressure phase diagram is constructed, which is shown in Figure 4.3(b). The direct evidence of the presence of the $Cu(NH_3)_2^+$ complex from XANES spectroscopy is shown in Figure 4.3(a).

The operando XANES spectroscopy [110] clearly shows that the existence of the $Cu(NH_3)_2{}^+$ complex during SCR at low temperature (150 °C). However, the signature for the $Cu(NH_3)_2{}^+$ complex disappears when the temperature is increased to 250 °C. Generally, the temperature is within 100 to 200 °C and the NH_3 concentration is $\sim$ 300-500 ppm for low-temperature NH_3-SCR. From the phase diagram (Figure 4.3(b)), it is clear that $Cu(NH_3)_2{}^+$ is the preferable species during the low-temperature regime. The phase-diagram also shows that a temperature increase leads to sequential desorption of ammonia although the region with only one ligand is narrow. Cu(I) is bonded directly to the framework at high temperatures. The detailed structural information on the relevant structures are shown in **Paper II**. This identification of NH_3–solvated Cu-ions is important as it suggests that the character of the active sites depends on the operating conditions.

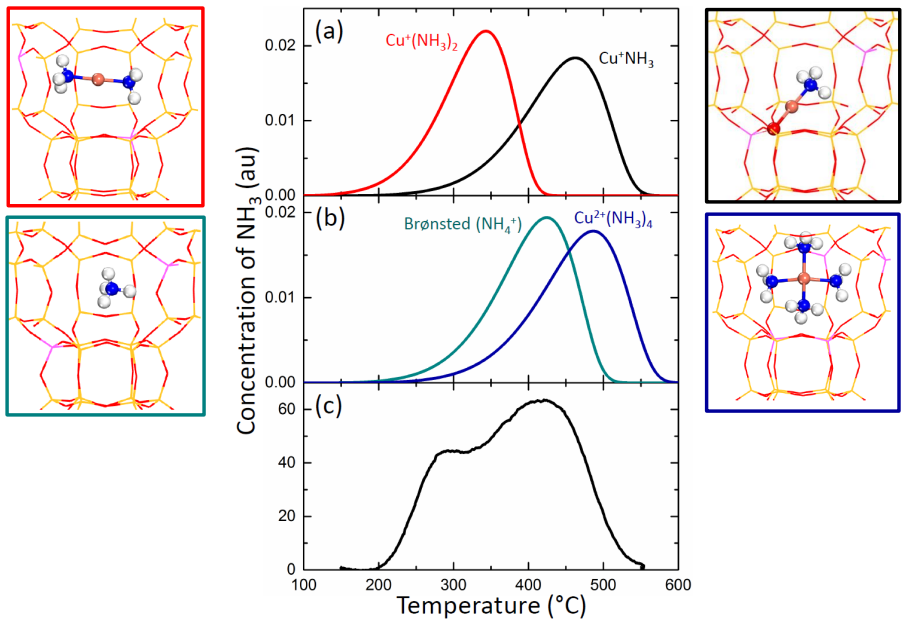

Figure 4.4: (a and b) Simulated desorption profiles of NH_3 in Cu-CHA. The parent complexes are indicated. (c) Experimental NH_3-TPD profile after NH_3 adsorption in Cu-CHA at 200 °C. The experimental Cu-CHA is prepared with the Si/Al ratio of 15 and the Cu content is 2.6 wt%, which corresponds to a Cu/Al ratio of 0.47. The simulations and experiments are performed with a heating rate of 3 °C/min and a flow rate of 190 Nml/min.

4.3 Temperature-programmed desorption of ammonia

Temperature-programmed desorption of ammonia is widely used for zeolite characterization revealing information on the number and strength of acidic sites. The NH_3-TPD profile of Cu-CHA is generally characterized by three desorption peaks;[119–122] a low-temperature peak below 200 °C, an intermediate-temperature peak at 250-350 °C and a high-temperature peak at 400-500 °C. The low-temperature peak is generally assigned to NH_3 adsorbed on Lewis acid sites,[119–121] whereas the peak at 400-500 °C has been attributed to NH_3 adsorbed on Brønsted acid sites. NH_3 adsorbed at Cu-sites has been suggested to give rise to the intermediate-temperature peak at 250-350 °C.[119–121] The evidence of NH_3-solvated complexes under NH_3-SCR conditions should have consequences for the interpretation of NH_3-TPD profiles from Cu-CHA. In particular, the desorbed NH_3 should partly originate from NH_3-solvated Cu-complexes. In **Paper IV**, we were aiming to shed light on the assignment on the NH_3-TPD peaks over Cu-CHA using density functional theory calculations in combination with kinetic simulations.

For NH_3 adsorption in Cu-CHA, we have considered a range of species. The energy required for decomposition of NH_4^+ is calculated to be 1.46 eV, which is within the range (1.34-1.67 eV) measured for the NH_3 adsorption on Brønsted acid sites in H-ZSM-5.[123]

The desorption energies from $[Cu(I)(NH_3)_2]^+$ are 1.29 and 1.54 eV, respectively. The clear separation between the two energies should result in different peaks in the TPD profile. Cu^{2+} is considered with one to four NH_3 ligands. The highest desorption energy is obtained when going from four to three ligands. The sequential desorption energies for the remaining ligands are all lower. Thus, once the decomposition of the $Cu(II)(NH_3)_4{}^{2+}$ complex starts, all ligands should desorb. The situation is slightly more complex for $Cu(II)(OH)(NH_3)_3{}^+$, which shows a non-monotonous behaviour with the highest energy calculated for decomposition of the second NH_3 ligand. Thus, also this species should give rise to multiple peaks in the TPD profile.

Figure 4.4 shows the simulated NH_3-TPD profiles together with an experimental profile. Figure 4.4(a) shows the desorption profiles for the linear complex. The peak at 350 °C originates from decomposition of $Cu(I)(NH_3)_2{}^+$, whereas the higher desorption energy for the remaining NH_3 ligand yields a peak at about 460 °C. Figure 4.4(b) shows the desorption peaks from NH_4^+ (Brønsted acid site) and $Cu(II)(NH_3)_4{}^{2+}$ at 430 °C and 475 °C, respectively. As the desorption energies of the remaining NH_3 adsorbed on Cu^{2+} are lower than the first, only one peak should appear for this complex.

We compare the simulated TPD profiles with an experiment performed for Cu-CHA (Figure 4.4(c)). The experiment was performed with NH_3 adsorbed at 200 °C. The temperature was lowered to 150 °C before starting the TPD measurement. The results show the two features at 290 and 430 °C, respectively. Based on the calculations, we attribute the lower temperature feature to the decomposition of $Cu(I)(NH_3)_2{}^+$. The feature at higher temperature could be assigned to $Cu(I)NH_3{}^+$, Brønsted acid sites (NH_4^+), and decomposition of $Cu(II)(NH_3)_4{}^{2+}$.

Chapter 5

Reaction mechanism for low temperature NH_3-SCR

5.1 Current understanding

Low-temperature NH_3-SCR follows either the standard or the fast NH_3-SCR scheme discussed in Chapter 1. During standard NH_3-SCR, an oxygen molecule needs to dissociate, whereas NO_2 is involved in the fast NH_3-SCR reaction. It has experimentally been shown that the NH_3-SCR reaction proceeds via alternating reduction and oxidation steps.[15] In the reduction step, Cu ions are reduced from Cu(II) to Cu(I), whereas Cu(I) is reoxidized to Cu(II) in the oxidation step. It is generally believed that oxygen dissociation is a key step during standard NH_3-SCR at temperatures below 250 °C.[22;30;31] Given the emerging picture that copper ions at low temperatures are solvated by NH_3 during typical SCR-conditions, it becomes important to explore whether $Cu(NH_3)_2^+$ can act as sites for O_2 activation.

The apparent activation energy for low-temperature NH_3-SCR has been measured to be in a span from 0.4 to 0.8 eV,[30;121;124] which depends on the copper loading. However, the barrier for direct dissociation of O_2 over a single $Cu(NH_3)_2^+$ complex in CHA has been calculated to be over 2 eV.[37] Although NO is found be able to assist O_2 dissociation, the barrier for the dissociation over a single $Cu(NH_3)_2^+$ complex is still as high as 1.1 eV.[30] This indicates that O_2 is not dissociated over single Cu-cations but instead over some other species. The reaction has been measured to have a quadratic dependence on the copper loading at low Cu loadings,[30;31;125] which has been related to the second order behavior of the oxidation of Cu(I) to Cu(II) with respect to O_2. These results indicate that the standard SCR reaction at low temperature involves two Cu-sites, which implies that O_2 dissociation could proceed over a pair of $Cu(NH_3)_2^+$ complexes. Furthermore, up to $\sim$ 80% of Cu(I) in the form of $Cu(NH_3)_2^+$ has been suggested to be oxidized to Cu(II) by O_2 at 200 °C.[31] The pair formation of Cu sites relies on a high mobility of $Cu(NH_3)_2^+$ complexes, which is consistent with a low inter-cage diffusion barrier.[31;57]

The observations that Cu(I) ions are present as mobile ions solvated by NH_3 and that dissociation of oxygen requires a pair of Cu(I) ions, have changed the view of the NH_3-SCR reaction in Cu-CHA. As discussed in Chapter 1, a consistent reaction mechanism was proposed by Janssens *et al.*,[22] and selected intermediates were considered on framework-bonded copper sites. Dissociation of O_2 was in this case assisted by NO on an isolated framework-bonded copper site. Thus, this mechanism is not really applicable for low-temperature NH_3-SCR but could instead elucidate high-temperature NH_3-SCR. Even though a possible reaction cycle over solvated Cu(I) was proposed in Ref. [30] and the pair of $Cu(NH_3)_2^+$ complexes was considered as the active sites, the direct O_2 dissociation

was not considered, instead, an NO-assisted O_2 dissociation path was proposed.

To increase the understanding of low-temperature NH_3-SCR over Cu-CHA, it is crucial to develop a complete catalytic cycle based on the new insights. As a first step, the reaction path for direct O_2 dissociation over the $Cu(NH_3)_2^+$-pair in CHA is discussed. It is found that the reaction landscape for direct O_2 dissociation is strongly dependent on the choice of the xc-functional. A reasonable functional is determined by comparison to reference systems and it is found that O_2 is activated rather than dissociated. In a second step, the Al-distribution is found to affect the probability for the pair formation, which affects the probability for low-temperature O_2 activation. Lastly, a full catalytic NH_3-SCR cycle over Cu-CHA is proposed and the reaction is found to proceed in a multi-site fashion over both the copper complexes and the Brønsted acid sites.

5.2 Functional-dependent reaction landscape for O_2 activation

Although generalized gradient approximations (GGAs) successfully can describe molecular adsorption on the transition metal surfaces[126;127], these functionals normally underestimate the formation energies of oxides in part due to the overbinding of O_2 in the gas phase.[128;129] This error can be partly attributed to the incomplete cancellation of Coulomb and exchange interactions of an electron with itself in GGAs. The description of catalytic reaction in porous zeolite structures with DFT is challenging because different types of bonds should be described simultaneously with appropriate accuracy.[130] Related to the current system, the functional should describe the O_2 activation over the $Cu(NH_3)_2^+$-pair in CHA together with the Cu–N and Cu–O bonds. Additionally, the functional should account for the weak van der Waals (vdW) interactions with the zeolite framework.

Recent studies[30;31;131] have addressed O_2 dissociation over $Cu(NH_3)_2^+$ complexes with DFT calculations using different exchange-correlation functionals. The reported PES appear to depend strongly on the functional. The performance of the different functionals for this reaction is difficult to assess due to the lack of clear comparisons between calculated and experimental data. To understand the origin of different PES with different functionals and simultaneously establish a preferred functional for DFT calculations of Cu-CHA systems, eight functionals with three common approaches to account for vdW interactions have been explored in **Paper V**, namely (i) PBE with D2 and D3 corrections, (ii) BEEF-vdW and (iii) the vdW-density functional PBE+cx.

The potential energy landscape for direct O_2 dissociation on a $Cu(NH_3)_2^+$-pair in CHA calculated with different functionals is shown in Figure 5.1. The oxygen dissociation path is divided into steps with five structures denoted C1 to C5. It is clear that calculations with the different functionals result in different reaction paths and also reaction products. In general, all functionals indicate that Cu-pairs are favorable for oxygen adsorption. However, some of the PBE-based functionals predict the dissociated molecule (C5) to be the stable configuration, whereas BEEF, PBE+U, PBE+U+D3 and HSE06+D3 favor activated O_2 (C4). In the C4 configuration, both Cu-ions are bonded to two oxygen atoms in a symmetric way. This $Cu_2O_2^{2+}$ motif will be referred as "side-on". It is exothermic for all functionals to form the activated O_2 (C4) from C1, although BEEF results in a slightly endothermic step. O_2 dissociation is completed in the step from C4 to C5. The motif of dissociated O_2 over Cu pairs will be denoted as "bis". The energetics of C5 is found to be

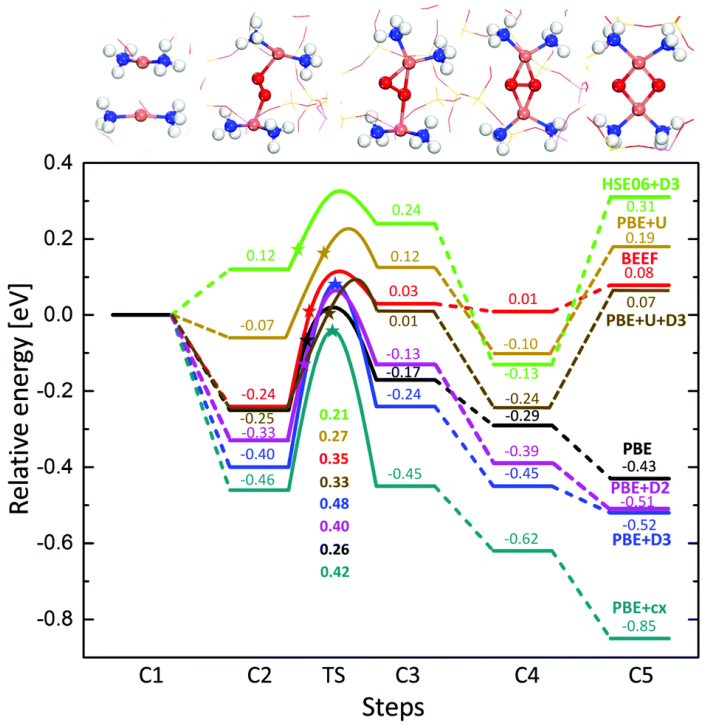

Figure 5.1: The potential energy landscape of direct O_2 dissociation on $Cu(NH_3)_2^+$-pairs in CHA calculated by different functionals. The structure for each step is shown at the top. The triplet to singlet transition for O_2 occurs between C2 and C3. TS stands for the transition state from C2 to C3 and the barriers are listed below the curves with the corresponding colors. The stars in the potential energy landscape denote the triplet to singlet transition. This figure is adapted from **Paper V**. Atom color codes: copper (pink), aluminum (purple), nitrogen (blue), silicon (yellow), oxygen (red) and hydrogen (white).

strongly functional dependent. The process is predicted to be endothermic by HSE06+D3, PBE+U, BEEF and PBE+U+D3, whereas it is exothermic in PBE, PBE+D2, PBE+D3 and PBE+cx. It is found that C4 is anti-ferromagnetic with a d^9 configuration for the copper ions whereas the C5-structure is a closed-shell system with zero magnetic moment. Figure 5.2(a) shows the spin density of the side-on isomer obtained by the PBE+U+D3 method. It clearly reveals the electron hole localized in the Cu d_{xy} orbital.

To investigate whether the large dependency of the PES on the functionals is attributed to the incorporation of vdW interaction with zeolites framework, the reaction of $Cu(NH_3)_2^+$ with oxygen in the gas phase is studied with different vdW approaches. The spatial confinement in the zeolite cages is expected to give substantial vdW interactions with the Cu-complexes. The vdW interactions for all the functionals result in a stabilization of 0.5 ± 0.1 eV for C2, C4 and C5. This shows that the van der Waals contributions are similarly described by the functionals accounting for this interaction. The discrepancies

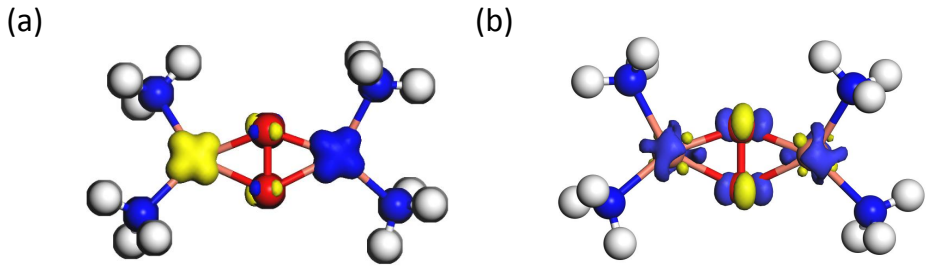

Figure 5.2: (a) Spin density of the side-on isomer by PBE+U+D3 method, blue and yellow isosurfaces show the alpha and beta spin orbitals, respectively; (b) The charge density difference (ρ(PBE+U+D3) - ρ(PBE+D3)) in the structure from PBE+U+D3 for the side-on configuration. The blue isosurface indicates charge gain and the yellow isosurface corresponds to charge depletion. The zeolites framework atoms in both cases are removed for clarity. Atom color codes: copper (pink), nitrogen (blue), oxygen (red) and hydrogen (white).

in the PES are instead related to different descriptions of the Cu-N or Cu–O chemical bonds. The sequential NH_3 binding energies in $Cu(NH_3)_x^+$ (x = 1-4) in gas phase are calculated with the different functionals and all functionals give reasonable descriptions compared with experimental values. Thus, it is the different descriptions of the Cu-O chemical bonds that makes the relative stability between side-on and bis Cu_2O_2 motifs different.

The Cu-O bonds in bulk copper oxides are known to be difficult to describe accurately with GGA-DFT[132;133]. The main reason is the strong correlation effects in systems with oxidized copper having highly localized 3d-states, which can not be accurately described within standard DFT methods. The determination of the relative energies between side-on and bis Cu_2O_2 motifs supported with NH_3 ligands is also challenging within *ab initio* wave-function based methods[134–136]. The fundamental reason for this is the large difference in the contributions of dynamical and nondynamical electron correlation effects to the total energies for the side-on and bis isomers.[135] In the side-on Cu_2O_2 motif, each Cu(II) has an unpaired electron and the system is a singlet. The configuration behaves like a singlet biradical and to give a correct description, at least two determinants are needed, which Kohn-Sham DFT does not provide.

Because of the lack of a direct benchmark to determine which functional that provides reasonable relative energies between side-on and bis, the electronic, structural and energetic properties of reference systems including bulk copper oxides and Cu_2O_2 enzymatic crystals are investigated in **Paper V**. It is found that PBE+U approach together with van der Waals corrections could provide a reasonable simultaneous accuracy of the different bonds in the systems. The employed Hubbard-U term is found to give a stabilization of the copper d-state in both copper oxides and the Cu_2O_2 motifs. The stabilized d-states influences the degree of delocalization and hybridization to the oxygen states and, consequently, the bonding. To exemplify how the Hubbard-U term affects the bonding, the charge

density difference between PBE+U+D3 and PBE+D3 is shown for C4 structure in Figure 5.2(b). The charge density difference shows that the inclusion of the Hubbard-U term localizes charge on the Cu ions. This rehybridization induces a polarization of the oxygen anions where charge is polarized towards the direction of the Cu-O bond. To support this analysis, the magnetic coupling constant (J) for the side-on structure is calculated using the broken symmetry approach.[137] The coupling constant in di-nuclear copper complexes is known to be sensitive to the degree of d-electron localization.[138;139] J is calculated to be -230 meV and -70 meV within PBE+D3 and PBE+U+D3, respectively. This demonstrates the increased d-electron localization when a Hubbard-U term is used, as the interaction between the two spins is reduced.

When the temperature increases above 300 °C, the NH_3 ligands will desorb from the $Cu(NH_3)_2^+$ complexes, which leads to an immobilized Cu^+ bound directly to the zeolite framework.[36–39;110] The dissociation of O_2 over the framework-bound Cu^+ is also found to require Cu^+-pairs, as the barrier for dissociation over a single cation is higher than $\sim$ 2 eV.[37;140] A possible reaction path for O_2 dissociation over the framework-bound Cu^+-pairs is shown in Figure 5.3. Each framework-bound Cu^+ is preferably located in the six-membered ring bridging two oxygen atoms (2Cu in Figure 5.3). This is in agreement with Refs[57;141;142]. To make it feasible to adsorb O_2, the two Cu^+ ions need to be close and the barrier for Cu^+ ion diffusion into the Cu-pair structure is 0.75 eV. The pair formation is endothermic by 0.4 eV. The O_2 adsorption over the Cu-pair is exothermic with respect to the reference. Once the O_2 is adsorbed, the reaction to CuOOCu is facile. As for the diamine complexes, we find that the complete dissociation is improbable.

It can be concluded from Figure 5.1 and 5.3 that the activation of O_2 proceeds with low barriers over both types of Cu pairs (NH_3 solvated Cu^+ and framework-bound Cu^+). However, the diffusion of framework-bound Cu^+ between adjacent cages is associated with a considerable barrier, which makes the Cu^+-pair formation less facile. The low probability of Cu^+-pair formation in the framework-bound Cu-CHA could lead to a lower heat release upon O_2 adsorption as compared to the $Cu(NH_3)_2^+$ complexes. In **Paper VII**, the heat of O_2 adsorption over $Cu(NH_3)_2^+$ complexes and the framework-bound Cu^+ species in CHA is measured by microcalorimetry. O_2 adsorption results in considerably higher heat release over the $Cu(NH_3)_2^+$ complexes than the framework-bound Cu^+ species, which is consistent with the results predicted by DFT calculations.

5.3 Effect of Al-distribution on O_2 activation

The flat PES for the O_2 activation over the $Cu(NH_3)_2{}^+$-pair shows that the reaction is facile. As each $Cu(NH_3)_2{}^+$ is associated with one Al site, it is of interest to know whether the formation of the $Cu(NH_3)_2{}^+$ pair is affected by the Al distribution in CHA. This was done in **Paper III** In particular, eight configurations have been selected to calculate the $Cu(NH_3)_2{}^+$-pair formation energy according to:

$$\Delta E_{form} = E_{\mathrm{2Cu@CHA}} + E_{\mathrm{H_2(gf)}} - E_{\mathrm{2H@CHA}} - E_{\mathrm{2Cu(gf)}} \tag{5.1}$$

where $E_{\mathrm{2Cu@CHA}}$ is the total energy of the $Cu(NH_3)_2{}^+$ pairs in the large cage, $E_{\mathrm{2H@CHA}}$ is the total energy of two protons in the CHA structure, $E_{\mathrm{H_2(gf)}}$ and $E_{\mathrm{2Cu(gf)}}$ are the

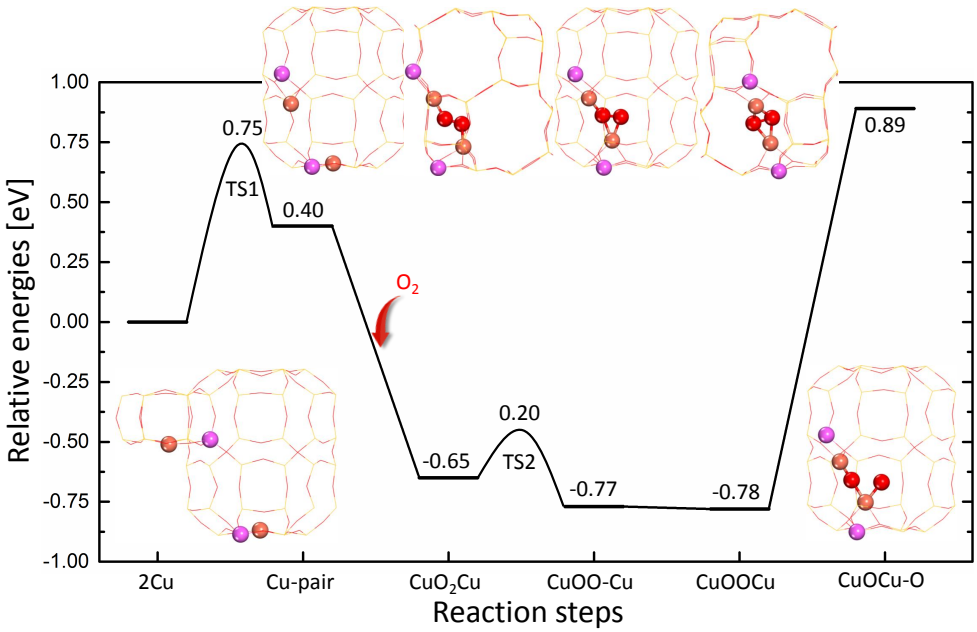

Figure 5.3: The potential energy landscape of direct O_2 dissociation over framework-bound Cu^+-pairs in CHA. The structures for each step are shown. For clarity, the CHA framework is kept as lines. Atom color codes: copper (pink), aluminum (purple), silicon (yellow) and oxygen (red).

total energy of hydrogen in gas phase and $Cu(NH_3)_2{}^+$ pairs in gas phase, respectively. Molecular dynamics are performed at 127 °C with 5 ps to sample the structures of the $Cu(NH_3)_2{}^+$ pairs in the large cage of CHA. $E_{2Cu@CHA}$ is calculated by geometry optimization of lowest energy structures selected from MD trajectories.

The CHA structure with a large and a small cage is shown in Figure 5.4(a). The eight configurations are shown in Figure 5.4(b). The eight configurations have gradually increased Al-Al distance from 4.5 to 13.8 Å. The Al-distribution has a negligible effect on the stability of the protons. However, the relative formation energies of the $Cu(NH_3)_2{}^+$ pairs (green line with circle symbols) have a large difference up to ~ 0.55 eV. Configuration 3 has the highest stability, whereas configuration 1 has the lowest stability. The other configurations (2, 6, 7 and 8) have similar stability (within 0.1 eV) but clearly not as stable as configurations 3, 4 and 5. Thus, we conclude that an Al-distribution such as configuration 1 yields a probability for the $Cu(NH_3)_2{}^+$ pair formation considerably lower than, for example, configuration 3.

Taking the low barrier for O_2 activation into account suggests that the low-temperature NH_3-SCR activity for Cu–CHA could be governed by the formation of $Cu(NH_3)_2{}^+$-pairs rather than by the O_2 activation. This indicates that it should be possible to improve the catalytic activity by precise control of the Al-distribution in the framework structure of the zeolite.

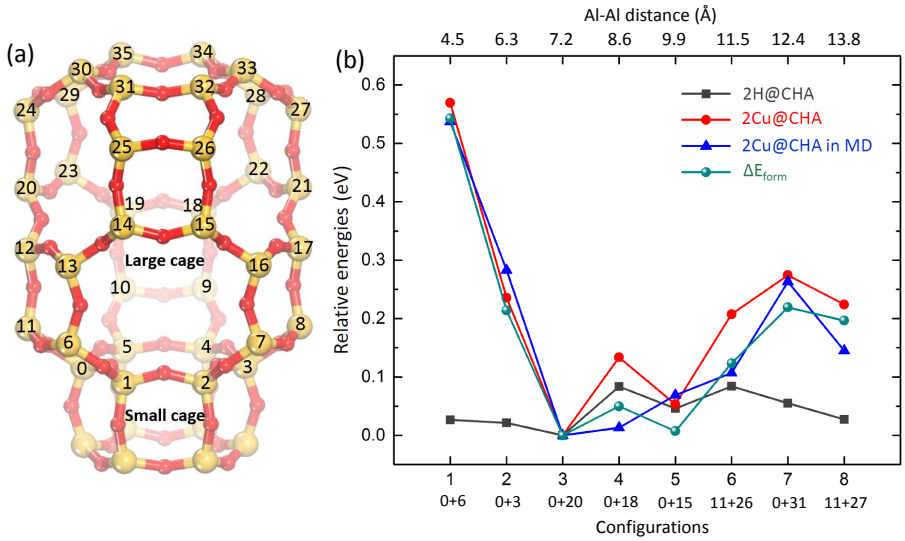

Figure 5.4: (a) The large and small cavity of the CHA structure. All Si atoms in the large cavity are marked with numbers to make the following statement easier on the replaced Al sites. (b) Relative energies of the eight configurations with two Si atoms replaced by two Al atoms. The numbers for the placement of the Al-atoms are indicated. The dark gray line with square symbols represents the total energies of two protons as Brønsted acid sites. The red line with circle symbols shows the total energies of the $Cu(NH_3)_2{}^+$ pairs in the large cage. The blue line with triangle symbols shows the average energies of the pairs in the large cage during each MD simulation. The green line with ball symbols shows the pair-formation energies for the eight configurations. All the energies are shown with respect to the corresponding energy of configuration 3. Atom color codes: silicon (yellow) and oxygen (red).

5.4 A complete multi-site reaction mechanism

The observations that Cu(I) ions are present as mobile ions solvated by NH_3 and that activation of oxygen requires a pair of Cu(I) ions, indicates that a reaction mechanism for the entire NH_3-SCR reaction over $Cu(NH_3)_2{}^+$ is required to increase the understanding of this reaction. In particular, it is important to clarify the role of the pairs in the catalytic cycle beyond the O_2 dissociation step, especially whether all reactions take place over the pair or if there is a dynamic interplay between reactions over pairs and single $Cu(NH_3)_2^+$ complexes. Another question regarding the reaction mechanism is the role of Brønsted acid sites. It has been shown that the NH_3-SCR rate depends linearly on the number of Brønsted acid sites per Cu site.[121] In this part, these questions will be discussed and a complete reaction mechanism will be presented.

5.4.1 Interplay between Cu sites and Brønsted acid sites

The starting point for the construction of the reaction cycle is a pair of $Cu(NH_3)_2^+$ complexes. Two possible cycles are proposed (see Figure 5.5), which share the route for oxygen activation but differ in the way NO adsorbs. In Cycle I, NO adsorbs on the Cu site, whereas it adsorbs on activated oxygen in Cycle II. In both cycles, O_2 is only activated because its complete dissociation is energetically unfavorable.

Two sites are involved in the reaction mechanism, *i.e.*, a Cu site and a Brønsted acid site. For both two cycles, HONO and H_2NNO species, which are important intermediates, are formed on Cu sites, whereas the decomposition of these species preferably proceeds on Brønsted acid sites. The PES for both cycles is shown in **Paper VI**, which shows that the reactions on Cu cites are facile with low barriers. The highest barrier (0.74 eV) is found for the H_2NNO decomposition over the Brønsted acid site including molecular reorientations. Note that this value can be considered as an upper bound as the molecular reorientations can be facilitated by additional neighboring Brønsted acid sites. The value is comparable with the measured apparent activation energies which are in a span from 0.4 to 0.8 eV.[30;121;124]

The complex pair is easily separated during the reaction cycle in both cycles. For Cycle I, the pair breaks between species F and G when both copper species are reduced to Cu(I). The separation for Cycle II occurs between species C and D giving NO_2 the possibility to adsorb in a bidentate manner on the copper ion. The facile formation and separation of the pair during the catalytic cycles underlines that structural flexibility is a fundamental property of the active site. During the reaction cycles, we find that the solvated Cu(I) and Cu(II)-sites are coordinated to oxide, hydroxide, and NO_x ligands. This is in agreement with infrared and X-ray absorption spectroscopy measurements, which have shown different types of mixed-ligand systems.[39;143]

The catalytic cycles have here been developed for the standard SCR reaction. In the presence of NO_2, an alternative is the fast SCR-reaction (Reaction 2 in Chapter 1), which proceeds without O_2 adsorption. Cycle II provides a suggestion for how this reaction can proceed over the NH_3-solvated Cu-species. In this case, the reaction takes place on a single copper complex, without the formation of Cu pairs. The adsorption of NO_2 gives a Cu^{2+} site where NO^+ can be formed. From here, the fast-SCR reaction follows the

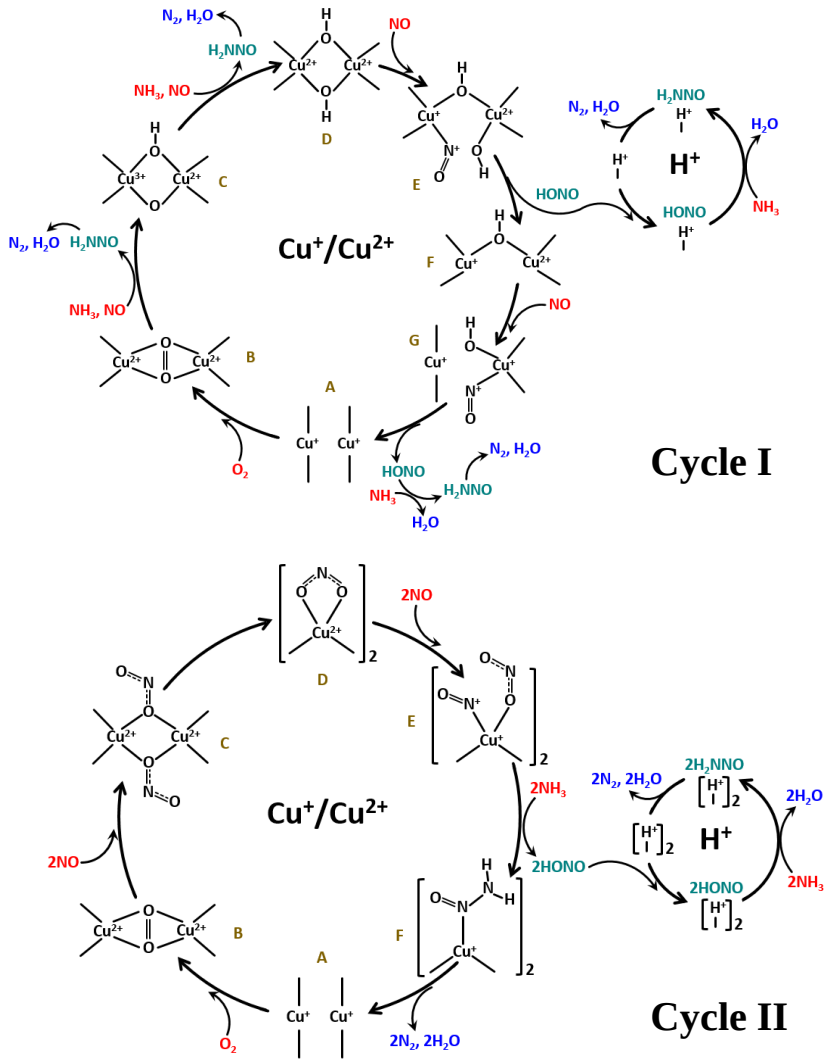

Figure 5.5: Two possible reaction cycles (Cycle I and II) for low-temperature NH_3-SCR over Cu-CHA. Each cycle contains reaction intermediates on the Cu^+/Cu^{2+} sites and on the H^+ site. Dangling sticks connected with the Cu ions indicate the NH_3 ligands. The reactants, the reaction intermediates and the products are indicated in red, green and blue, respectively.

same path as the standard NH_3-SCR reaction (Cycle II). The major difference between fast-SCR and standard-SCR is that the fast SCR cycle does not depend on pairing of copper-complexes, which is in agreement with experimental observations.[30;31]

5.4.2 On the selectivity in NH_3-SCR

The presented reaction mechanism highlights the dynamic character of Cu-sites and the need of a balanced Cu/H ratio in zeolites for low-temperature NH_3-SCR. The formation and separation of the $Cu(NH_3)_2^+$-pair, which are assisted by the NH_3-solvation, facilitate the reactions on the Cu sites. The intermediate species that are formed on the Cu sites, *i.e.*, HONO and H_2NNO, are found to be easily decomposed over the Brønsted acid sites via a series of proton exchange processes. The downhill PES (in **Paper VI**) of the two proposed reaction cycles shows that the reactions are facile.

There are mainly two undesirable reactions during NH_3-SCR as discussed in Chapter 1. One is NH_3 oxidation and the other is N_2O formation. We note that the activity of NH_3 oxidation has been measured to be low during the low-temperature NH_3-SCR over Cu-CHA.[144] The reason could be explained with the suggested reaction mechanism. From the proposed reaction cycles, the dehydrogenation of NH_3 occurs on activated oxygen species (Cycle I) or nitrite species (Cycle II) simultaneously to the N-N coupling between NH_2 and NO^+ forming H_2NNO. This simultaneous N-N coupling prevents the further dehydrogenation of NH_2 species to NH and N, which are the potential intermediates for NH_3 oxidation.[145] Moreover, all the NH_3 molecules on the copper sites are bent away from the oxygen atoms. Thus, from a geometric perspective, it is difficult to couple the NH_3 ligand and the activated oxygen atoms, which hinders the oxidation of the NH_3 ligand.

N_2O formation during the low-temperature NH_3-SCR over Cu-CHA has been considered as a major drawback of this catalyst.[18] Many studies have been carried out to investigate the mechanism for N_2O formation. It is generally believed that N_2O forms mainly from the decomposition of ammonium nitrate (NH_4NO_3) during low-temperature NH_3-SCR.[18;19;146] The N_2O production was found to increase when the NO_2 concentration is increased in the feed,[147–149] which is an indirect evidence that N_2O is formed via ammonium nitrate. It was also found that H_2O in low concentrations can facilitate N_2O formation, which was attributed to the increase in Brønsted acidity.[19] A formation mechanism for ammonium nitrate can be suggested on the basis of Cycle II. From Species B to C, nitrate species can be formed if only one NO is adsorbed on one activated oxygen atom. Actually, Figure 4(b) in **Paper II** provides a possible reaction path for the nitrate formation. Ammonium nitrate can be further formed upon the interaction between ammonium and nitrate. The Brønsted acid site could be regenerated by H_2O decomposition. The decomposition of ammonium nitrate is relatively fast for temperatures above 200 °C and at lower temperatures it can block the active sites or the pores in zeolites.[150] This can be one reason why the low-temperature "fast" NH_3-SCR reaction is not really fast compared with the standard NH_3-SCR reaction over Cu-exchanged small-pore zeolite.[151;152]

Chapter 6

Conclusions and outlook

The present thesis has attempted to provide understanding of the reaction mechanism for low-temperature NH_3-SCR reaction over Cu-CHA. This has been approached in two steps. In the first step, the nature of the active site under typical reaction conditions was investigated. In the second step, the full reaction mechanism on the $Cu(NH_3)_2^+$ complex was explored. The work has been performed by first principles calculations using density functional theory coupled with thermodynamics analysis.

In the first step, the character of the Cu ions in the presence of NH_3 was determined as a function of temperature. By constructing a temperature-pressure phase diagram for $Cu(NH_3)_x^+$, Cu ions were found to be solvated preferably by two NH_3 ligands forming a linear $Cu(NH_3)_2^+$ complex under low-temperature operating conditions, which refer to the temperatures between 100 and 200 °C and an NH_3 concentration between 300 and 500 ppm. Increasing temperature would lead to sequential desorption of ammonia from the Cu site, which results in a framework-bound Cu ion when the temperature exceeds 300 °C. The low barrier for the diffusion of the linear $Cu(NH_3)_2^+$ complex through the zeolites cages demonstrates the high mobility of the complex during the reaction condition. The high mobility of the $Cu(NH_3)_2^+$ complex was also found to be important for the functionalization of zeolites via solid-state ion-exchange, where the complex plays the role of a Cu-ion carrier. Further, the interaction between NH_3 and the acid sites (including Brønsted and Lewis acid sites) of the zeolite was studied by simulating temperature-programmed desorption profiles of NH_3 over Cu-CHA. It was found that the intermediate-temperature (250-350 °C) peak can be assigned to the desorption of NH_3 from the linear $Cu(I)(NH_3)_2^+$ complex and the high-temperature (400-500 °C) peak can be mainly assigned to the decomposition of NH_4^+ and $Cu(II)(NH_3)_4{}^{2+}$.

In the second step, a complete reaction mechanism for low-temperature NH_3-SCR over Cu-CHA was proposed. For the standard NH_3-SCR reaction, an oxygen molecule needs to adsorb. Direct O_2 activation was found to proceed over a $Cu(NH_3)_2^+$-pair with low barriers, which is consistent with the experimentally observed second order dependence of the reaction on the copper loading at low Cu loadings. The Al-distribution was found to affect the probability of the pair formation in a cage. Too far or too close Al-Al distances reduce the stability of the pair. The reaction landscape for direct O_2 dissociation was found to be strongly functional-dependent. Considering both computational costs and accuracy, PBE+U+D3 is found to be a reasonable compromise. With this functional, O_2 was found to be activated rather than dissociated over the $Cu(NH_3)_2^+$-pair.

Based on the fact that Cu(I) ions are present as $Cu(NH_3)_2^+$ complexes and a pair of these complexes is required for the direct O_2 activation, two possible reaction cycles are proposed, which share the route for oxygen activation but differ in the way NO adsorbs. Two types of sites, Cu and Brønsted acid sites, were found to be involved in the

reaction mechanism. After activating O_2, NH_3 can couple with an NO^+, which is formed upon the NO adsorption on Cu(II). The facile N-N coupling in both cycles can form the intermediate species, HONO and H_2NNO, which were found to easily decompose over the Brønsted acid sites via a series of proton exchange processes. The multi-site character of the reaction implies that catalysts should be synthesized with a balanced Cu/Al ratio. The proposed complete reaction mechanism is consistent with measured kinetic data from the literature and improves the current understanding of the NH_3-SCR reaction.

The work has highlighted some general challenges exploring zeolite reactions from first principles. One issue is the flat potential energy surface with many local minima of the species. Thus, a conventional geometry optimization strategy is not successful to obtain an estimation of the global minimum. In this work, *ab initio* molecular dynamics was performed to sample the potential energy surface. In this approach, the dynamic behavior of this system is captured by solving Newton's equations of motion at a certain temperature and several configurations are selected from the trajectories for further optimization. However, the reliability of molecular dynamics depends primarily on the length of the trajectories which are limited due to the computational cost. There are several alternative approaches to find low-energy structures, for example, Monte Carlo sampling,[153] Basin-Hopping algorithms[154] or Meta-dynamics.[155]

Although density functional theory has been successful in describing molecule-surface interactions in heterogeneous catalysis, the unphysical self-interaction error of commonly used exchange-correlation functionals is an issue for non-metal systems. The self-interaction error can be serious when dealing with highly localized d of f electrons in the oxidized transition metals. Although the use of a Hubbard-U term (DFT+U) is a feasible approach to correct for the self-interaction error, it is not straight forward to determine the value of the parameters, which strongly affect the results. Currently, two common ways are used to determine the numerical value of the parameter. One is to calculate some known properties of a system with selected values for U-parameters and to determine which value that gives a reasonable result. The other is to obtain the value self-consistently from *ab initio* calculations. The *ab initio* approach often gives a range of possible U parameters and does not always provide more reliable results than the method of fitting to some extent.[65;156] The ambiguities in determination of the U-values means that the DFT+U approach to some extent lacks robustness. Additionally, the U-value could, in principle, change during reaction. In the present case, different U-values might be required for different oxidation states of Cu. The investigated reaction has species with Cu(I), Cu(II) and Cu(III). Adding exact exchange energy from the Hartree-Fock approach to DFT in hybrid functionals is another approach to deal with the self-interaction error. However, also this approach has limitations connected to large computational cost and the unknown percentage of exact exchange that should be used.

One issue with the presented reaction is the spin-flip as O_2 is activated. Here the "Minimum Energy Crossing Point" was used to obtain the reaction barrier. This approach calculates the relative energy between potential energy surfaces corresponding to the different spin states. However, the kinetics of the spin flip from one potential energy surface to the other has not been considered. To determine the rate of the reaction, spin-orbital coupling must be considered to calculate the probability of changing the spin from triplet to singlet.

To obtain the free energy landscape for a catalytic reaction in a zeolite cage, the entropy change should be properly calculated. It should be noted that the harmonic approximation underestimates the entropies of the molecules in the cage as the retained translational and rotational degrees of freedom are not properly described. There are tentative estimations that assume that one[38] or two[157] translational degrees of freedom are lost for molecules entering a zeolite cage. Using Monte Carlo simulations, it has previously been estimated that the rotational and translational entropy in zeolite cages are about half of that in the gas phase.[158] Entropy changes during reactions in zeolites should preferably be done accounting for non-harmonic effects.[159–161]

In this work, two possible reaction cycles for low-temperature NH_3-SCR are proposed. Although the proposed reaction mechanism is consistent with the measured kinetic data, other paths could be possible. One example is the role of water as water is abundant in zeolites. For example, the relatively facile deprotonization of H_2O in zeolites may assist the decomposition of the intermediate species HONO and H_2NNO. The interactions between H_2O and Cu ions could also affect the redox reactions proceeding on the Cu sites.

This thesis suggests a complete reaction mechanism for low-temperature NH_3-SCR over Cu-CHA, which provides a solid basis for future investigations in the NH_3-SCR area. The thesis has also exemplified challenges with describing zeolite reactions from first principles. It shows that the field needs detailed comparisons between experiments and theoretical studies both for interpretation of experimental data and for benchmarking the computational methods.

Acknowledgments

The research work in this thesis was carried out at the Division of Chemical Physics at the Department of Physics and the Competence Centre for Catalysis (KCK) at Chalmers University of Technology, Göteborg, Sweden, from August 2015 to December 2019.

This research is financially supported by the Swedish Energy Agency and the member companies AB Volvo, ECAPS AB, Johnson Matthey AB, Preem AB, Scania CV AB, Umicore AG & Co. KG, Volvo Car Corporation AB and Wärtsilä Finland Oy. Additional financial support from the Swedish Research Council and the Chalmers Area of Advance Transport is acknowledged. The calculations have been performed at C3SE (Göteborg) and PDC (Stockholm) through a SNIC grant.

Additionally, I would like to express my sincere gratitude to:

My main supervisor, Henrik Grönbeck, for your patient guidance, motivation and advices throughout my PhD studies. Although there were some difficulties, for examples, hard tasks in the research work or tough questions from reviewers, you have always given me valuable insights on how to deal with the issues. I also appreciate your encouragement on my independent thinking, which have given me confidence. Nearly one hundred percent availability to reach you in your office have made it possible to solve my scientific queries promptly, for which I am grateful. Without your careful reading and detailed feedback this PhD thesis would not have been achievable.

My co-supervisors, Magnus Skoglundh and Anders Hellman, for your constant support of my project. Magnus, thanks for your insightful ideas and constructive suggestions on the work presented in the thesis. Your encouragement on my project both in kind and humorous ways boosted my confidence. Anders, thanks for your advices on my thesis and also thanks for being so approachable all the time, specially when we first met during the interview, which relieved my nerves.

My collaborators, Ton V.W. Janssens, Jonas Jansson, Xueting Wang and Hanne Falsig. Ton, thanks for your efforts in our collaborations. Although there were always hard questions from you, they indeed improved our understanding and also made the manuscripts more comprehensive. Jonas, thanks for all discussions we have had and also thanks for your suggestions on the work, which have been very helpful. Ting, thanks for being always so patient to respond to my questions in our collaboration. It has been very enjoyable to learn from the experimental perspective. Hanne, thanks for all discussions we have had and also thanks for your efforts in our collaborations.

All my colleagues at Chemical Physics for creating a friendly working environment. In particular, I would like to thank the past and present people in our theoretical group: Adam, Alvaro, Baochang, David, Lucy, Maxime, Mikael, Mikkel, Noemi, Philip, Unni

and Yingxin. I also would like to thank Christopher, Irem, Iwan, Joel and Johan for the fun time we have had.

All KCK members for your sharing results and ideas. Thank you!

I also want to thank my spot in the office F5119, where I have worked almost for four years. The orientation of my desk helps me to concentrate on my work, or sometimes music, and the view from the window in front of my desk have given me a pleasant state of mind. My spot is the best from my point of view.

Last but not least, I want to thank my parents and Qing. Baba and Mama (Chinese pronunciation for Dad and Mom), thank you for your encouragement and supports both on life and study aspects and for the ways that guide me to find my interests. Qing, thank you for your love and support, without which I would not have come this far.

Bibliography

[1] J. K. Smith. *History of catalysis*. Wiley, 2010. ISBN 978-0471227618.

[2] M. Beller, A. Renken, and R. A. Santen. *Catalysis: from principles to applications*. Wiley, 2012. ISBN 978-3527323494.

[3] J. K. Casper. *Fossil fuels and pollution: the future of air quality*. Facts on File, 2010. ISBN 978-0816072655.

[4] European Environment Agency (EEA). National emissions reported to the Convention on Long-range Transboundary Air Pollution (LRTAP Convention). Technical report, European Environment Agency (EEA), 2011.

[5] M. Koebel, M. Elsener, and M. Kleemann. Urea-SCR: a promising technique to reduce NOx emissions from automotive diesel engines. *Catalysis today*, 59:335–345, 2000.

[6] M. Zheng, G. T. Reader, and J. G. Hawley. Diesel engine exhaust gas recirculation — a review on advanced and novel concepts. *Energy Conversion and Management*, 45:883–900, 2004.

[7] R. Burch. Knowledge and know - how in emission control for mobile applications. *Catalysis Reviews*, 46:271–334, 2004.

[8] T. Kobayashi, T.Yamada, and K.Kayano. Effect of basic metal additives on NO_x reduction property of Pd-based three-way catalyst. *Appl. Catal., B*, 30:287–292, 2001.

[9] P. Granger and V. I. Parvulescu. Catalytic NO_x abatement systems for mobile sources: from three-way to lean burn after-treatment technologies. *Chemical Reviews*, 111:3155–3207, 2011.

[10] J. Wang, H. Chen, Z. Hu, M. Yao, and Y. Li. A review on the Pd-based three-way catalyst. *Catalysis Reviews*, 57:79–144, 2015.

[11] M. Takeuchi and S.I. Matsumoto. NO_x storage-reduction catalysts for gasoline engines. *Topics in catalysis*, 28:151–156, 2004.

[12] S. Roy and A. Baiker. NO_x storage−reduction catalysis: from mechanism and materials properties to storage−reduction performance. *Chemical Reviews*, 109: 4054–4091, 2009.

[13] L. Lietti, P. Forzatti, I. Nova, and E. Tronconi. NO_x storage reduction over Pt-Ba/γ-Al_2O_3 catalyst. *Journal of catalysis*, 204:175–191, 2001.

[14] R. Mrad, A. Aissat, R. Cousin, D. Courcot, and S. Siffert. Catalysts for NO_x selective catalytic reduction by hydrocarbons (HC-SCR). *Applied Catalysis A: General*, 504:542–548, 2015.

[15] F. Gao, J. H. Kwak, J. Szanyi, and C. H. Peden. Current understanding of Cu-exchanged chabazite molecular sieves for use as commercial diesel engine $DeNO_x$ catalysts. *Topics in Catalysis*, 56:1441–1459, 2013.

[16] A. M. Beale, F. Gao, I. Lezcano-Gonzalez, C. H. Peden, and J. Szanyi. Recent advances in automotive catalysis for NO_x emission control by small-pore microporous materials. *Chemical Society Reviews*, 44:7371–7405, 2015.

[17] E. Borfecchia, P. Beato, S. Svelle, U. Olsbye, C. Lamberti, and S. Bordiga. Cu-CHA – a model system for applied selective redox catalysis. *Chemical Society Reviews*, 47: 8097–8133, 2018.

[18] S. Brandenberger, O. Kröcher, A. Tissler, and R. Althoff. The state of the art in selective catalytic reduction of NO_x by ammonia using metal-exchanged zeolite catalysts. *Catalysis Reviews*, 50:492–531, 2008.

[19] D. Zhang and R.T. Yang. N_2O formation pathways over zeolite-supported Cu and Fe catalysts in NH_3-SCR. *Energy & fuels*, 32:2170–2182, 2018.

[20] R. H. Gonzales. Diesel exhaust emission system temperature test. Technical report, U.S. Department of Agriculture, 2008.

[21] A. J. Shih. *Synthesis and characterization of copper-exchanged zeolite catalysts and kinetic studies on NO_x selective catalytic reduction with ammonia.* PhD thesis, Purdue University, 2019.

[22] T. V. W. Janssens, H. Falsig, L. F. Lundegaard, P. N. R. Vennestrøm, S. B. Rasmussen, P. G. Moses, F. Giordanino, E. Borfecchia, K. A. Lomachenko, C. Lamberti, and S. Bordiga. A consistent reaction scheme for the selective catalytic reduction of nitrogen oxides with ammonia. *ACS Catalysis*, 5:2832–2845, 2015.

[23] A. Scheuer, M. Votsmeier, A. Schuler, J. Gieshoff, A. Drochner, and H. Vogel. NH_3-slip catalysts: experiments versus mechanistic modelling. *Top. Catal.*, 52: 1847–1851, 2009.

[24] I. Nova and E. Tronconi. *Urea-SCR technology for deNOx after treatment of diesel exhausts.* Springer, 2014. ISBN 978-1489980717.

[25] M. E. Davis and R. F. Lobo. Zeolite and molecular sieve synthesis. *Chem. Mater.*, 4:756—-768, 1992.

[26] M.E. Davis. Ordered porous materials for emerging applications. *Nature*, 417: 813—821, 2002.

[27] A. M. Frey, S. Mert, J. Due-Hansen, R. Fehrmann, and C.H. Christensen. Fe-BEA Zeolite Catalysts for NH_3-SCR of NO_x. *Catal. Lett.*, 130:1–8, 2009.

[28] S. Brandenberger, O. Kröcher, A. Tissler, and R. Althoff. The State of the Art in Selective Catalytic Reduction of NO_x by Ammonia Using Metal-Exchanged Zeolite Catalysts. *Cat. Rev. - Sci. Eng.*, 50:492–531, 2008.

[29] J. H. Kwak, R. G. Tonkyn, D. H. Kim, J. Szanyi, and C. H. Peden. Excellent activity and selectivity of Cu-SSZ-13 in the selective catalytic reduction of NO_x with NH_3. *J. Catal.*, 275:187–190, 2010.

[30] F. Gao, D. Mei, Y. Wang, J. Szanyi, and C.H. Peden. Selective catalytic reduction over Cu/SSZ-13: linking homo- and heterogeneous catalysis. *Journal of the American Chemical Society*, 139:4935–4942, 2017.

[31] C. Paolucci, I. Khurana, A.A. Parekh, S. Li, A.J. Shih, H. Li, J.R.D. Iorio, J.D. Albarracin-Caballero, A. Yezerets, J.T. Miller, W.N. Delgass, F.H. Ribeiro, W.F. Schneider, and R. Gounder. Dynamic multinuclear sites formed by mobilized copper ions in NO_x selective catalytic reduction. *Science*, 357:898–903, 2017.

[32] E.I. Solomon, D.E. Heppner, E.M. Johnston, J.W. Ginsbach, J. Cirera, M. Qayyum, M.T. Kieber-Emmons, C.H. Kjaergaard, R.G. Hadt, and L. Tian. Copper active sites in biology. *Chem. Rev*, 114:3659–3853, 2014.

[33] V.I. Pârvulescua, P. Grangeb, and B. Delmonb. Catalytic removal of NO. *Catalysis Today*, 46:233–316, 1998.

[34] K. Kamasamudram, N.W. Currier, X. Chen, and A. Yezerets. Overview of the practically important behaviors of zeolite-based urea-SCR catalysts, using compact experimental protocol. *Catalysis Today*, 151:212–222, 2010.

[35] A. Wang, Y. Chen, E.D. Walter, N.M. Washton, D. Mei, T. Varga, Y. Wang, J. Szanyi, Y. Wang, C.H. Peden, and F. Gao. Unraveling the mysterious failure of Cu/SAPO-34 selective catalytic reduction catalysts. *Nat. Commun.*, 10:1137, 2019.

[36] A. Marberger, A.W. Petrov, P. Steiger, M. Elsener, O. Kröcher, M. Nachtegaal, and D. Ferri. Time-resolved copper speciation during selective catalytic reduction of NO on Cu-SSZ-13. *Nature Catalysis*, 1:221–227, 2018.

[37] L. Chen, H. Falsig, T.V.W. Janssens, and H. Grönbeck. Activation of oxygen on $(NH_3\text{-Cu-}NH_3)^+$ in NH_3-SCR over Cu-CHA. *Journal of Catalysis*, 358:179–186, 2018.

[38] C. Paolucci, A. A. Parekh, I. Khurana, J. R. Di Iorio, H. Li, J. D. Albarracin Caballero, A. Shih, T. Anggara, W. N. Delgass, J. T. Miller, and F. H. Ribeiro. Catalysis in a cage: condition-dependent speciation and dynamics of exchanged Cu cations in SSZ-13 zeolites. *J. Am. Chem. Soc.*, 138:6028–6048, 2016.

[39] F. Giordanino, E. Borfecchia, K. A. Lomachenko, A. Lazzarini, G. Agostini, E. Gallo, A. V. Soldatov, P. Beato, S. Bordiga, and C. Lamberti. Interaction of NH_3 with Cu-SSZ-13 catalyst: a complementary FTIR, XANES, and XES study. *J. Phys. Chem. Lett.*, 5:1552–1559, 2014.

[40] M. Born and R. Oppenheimer. Zur quantentheorie der molekeln. *Ann. Phys.*, 389: 457–484, 1927.

[41] E. Schrödinger. Quantisierung als eigenwertproblem. *Annalen der Physik*, 385: 437–490, 1926.

[42] D. R. Hartree. The wave mechanics of an atom with a non-coulomb central field. Part I. theory and methods. *Proc. Cambridge. Phil. Soc.*, 24:89–110, 1928.

[43] J. C. Slater. The self consistent field and the structure of atoms. *Phys. Rev.*, 32: 339–348, 1928.

[44] S. Nordholm, W. Eek, G. Nyman, and G. Bacskay. *Kvantmekanik för kemister.* Studentlitteratur, 2009. ISBN 978-9144015392.

[45] R. M. Martin. *Electronic structure: basic theory and practical methods.* Cambridge University Press, 2008. ISBN 0521534402, 978-0521534406.

[46] W. Koch and M.C. Holthausen. *A chemist's guide to density functional theory.* Wiley-VCH, 2001. ISBN 978-3-527-30372-4.

[47] L. H. Thomas. The calculation of atomic fields. *Proc. Cambridge. Phil. Soc.*, 23: 542–548, 1927.

[48] E. Fermi. Un Metodo Statistico per la Determinazione di alcune Prioprietà dell'Atomo. *Rend. Accad. Naz. Lincei.*, 6:602–607, 1927.

[49] P. Hohenberg and W. Kohn. Inhomogeneous electron gas. *Phys. Rev.*, 136:B864–B871, 1964.

[50] Y. He, J. Gräfenstein, E. Kraka, and D. Cremer. What correlation effects are covered by density functional theory? *Mol. Phys.*, 98:1639–1658, 2000.

[51] W. Kohn and L. J. Sham. Self-consistent equations including exchange and correlation effects. *Phys. Rev.*, 140:A1133–A1138, 1965.

[52] S. Kurth and J.P. Perdew. Role of the exchange–correlation energy: nature's glue. *Int. J. Quantum Chem.*, 77:814–818, 2000.

[53] O. Gunnarsson and B.I. Lundqvist. Exchange and correlation in atoms, molecules, and solids by the spin-density-functional formalism. *Phys. Rev. B*, 13:4274–4298, 1976.

[54] J. P. Perdew, K. Burke, and Y. Wang. Generalized gradient approximation for the exchange-correlation hole of a many-electron system. *Phys. Rev. B*, 54:16533, 1996.

[55] J. P. Perdew, K. Burke, and M. Ernzerhof. Generalized gradient approximation made simple. *Phys. Rev. Lett.*, 77:3865–3868, 1996.

[56] A. D. Becke. Density-functional exchange-energy approximation with correct asymptotic behavior. *Phys. Rev. A*, 38:3098–3100, 1988.

[57] L. Chen, J. Jansson, M. Skoglundh, and H. Grönbeck. Mechanism for solid-state ion exchange of Cu^+ into zeolites. *J. Phys. Chem. C*, 120:29182–29189, 2016.

[58] J. Kohanoff. *Electronic structure calculations for solid and molecules*. Cambridge University Press, 2006. ISBN 978-0521815918.

[59] A. D. Becke. A New Mixing of Hartree-Fock and Local Density-Functional Theories. *J. Chem. Phys.*, 98:1372–1377, 1993.

[60] J. Heyd, G.E. Scuseria, and M. Ernzerhof. Hybrid functionals based on a screened Coulomb potential. *J. Chem. Phys.*, 118:8207–8215, 2003.

[61] A.V. Krukau, O.A. Vydrov, A.F. Izmaylov, and G.E. Scuseria. Influence of the exchange screening parameter on the performance of screened hybrid functionals. *J. Chem. Phys.*, 125:224106, 2006.

[62] J. Hubbard. Electron correlations in narrow energy bands - IV. The atomic representation. *Proc. Roy. Soc. London*, 285:542, 1965.

[63] A. Rohrbach, J. Hafner, and G. Kresse. Electronic correlation effects in transition-metal sulfides. *J. Phys. Condens. Matter.*, 15:979–996, 2003.

[64] O. Bengone, M. Alouani, P. Blöchl, and J. Hugel. Implementation of the projector augmented-wave LDA+ U method: Application to the electronic structure of NiO. *Phys. Rev. B*, 62:16392, 2000.

[65] M. Cococcioni and S. De Gironcoli. Linear response approach to the calculation of the effective interaction parameters in the LDA + U method. *Phys. Rev. B*, 71: 035105, 2005.

[66] H.J. Kulik, M. Cococcioni, D.A. Scherlis, and N. Marzari. Density functional theory in transition-metal chemistry: A self-consistent Hubbard U approach. *Phys. Rev. Lett.*, 97:103001, 2006.

[67] S. Grimme. Accurate description of van der Waals complexesby density functional theory including empirical corrections. *J. Comp. Chem.*, 25:1463–1473, 2004.

[68] S. Grimme. Semiempirical GGA-Type density functional constructed with a long-range dispersion correction. *J. Comp. Chem.*, 27:1787–1799, 2006.

[69] S. Grimme, S. Ehrlich, and L Goerigk. A consistent and accurate ab initio parametrization of density functional dispersion correction (DFT-D) for the 94 elements H-Pu. *J. Comp. Chem.*, 132:154104, 2010.

[70] S. Grimme, S. Ehrlich, and L Goerigk. Effect of the damping function in dispersion corrected density functional theory. *J. Comp. Chem.*, 32:1456–1465, 2011.

[71] J. J. Mortensen, K. Kaasbjerg, S. L. Frederiksen, J. K. Nørskov, J. P. Sethna, and K. W. Jacobsen. Bayesian error estimation in density functional theory. *Phys. Rev. Lett.*, 95:216401, 2005.

[72] K. Lee, É.D. Murray, L. Kong, B.I. Lundqvist, and D.C. Langreth. Higher-accuracy van der Waals density functional. *Phys. Rev. B*, 82:8207–8215, 2010.

[73] J. Wellendorff, K. T. Lundgaard, A. Møgelhøj, V. Petzold, D. D. Landis, J. K. Nørskov, T. Bligaard, and K. W Jacobsen. Density functionals for surface science: exchange-correlation model development with Bayesian error estimation. *Phys. Rev. B*, 85:235149, 2012.

[74] H. Rydberg, B.I. Lundqvist, D.C. Langreth, and M. Dion. Tractable nonlocal correlation density functionals for flat surfaces and slabs. *Phys. Rev. B*, 62:6997–7006, 2000.

[75] H. Rydberg, M. Dion, N. Jacobson, E. Schröder, P. Hyldgaard, S. I. Simak, D. C. Langreth, and B. I. Lundqvist. Van der Waals density functional for layered structures. *Phys. Rev. Lett.*, 91:126402, 2003.

[76] M. Dion, H. Rydberg, E. Schröder, D. C. Langreth, and B. I. Lundqvist. Van der Waals density functional for general geometries. *Phys. Rev. Lett.*, 92:246401, 2004.

[77] T. Thonhauser, V.R. Cooper, S. Li, A. Puzder, P. Hyldgaard, and D.C. Langreth. Van der Waals density functional: Self-consistent potential and the nature of the van der Waals bond. *Phys. Rev. B*, 76:125112, 2007.

[78] K. Berland and P. Hyldgaard. Exchange functional that tests the robustness of the plasmon description of the van der Waals density functional. *Phys. Rev. B*, 89: 035412, 2014.

[79] D. S. Sholl and J. A. Steckel. *Density functional theory: a practical introduction.* Wiley-Interscience, 2009. ISBN 978-0470373170.

[80] P. E. Blöchl. Projector Augmented-Wave Method. *Phys. Rev. B*, 50:17953–17979, 1994.

[81] G. Kresse and D. Joubert. From Ultrasoft Pseudopotentials to the Projector Augmented-Wave Method. *Phys. Rev. B*, 59:1758–1775, 1999.

[82] J. M. Thomas and W. J. Thomas. *Principles and practice of heterogeneous catalysis.* Wiley VCH, 1996. ISBN 978-3527292394.

[83] M. Jørgensen and H. Grönbeck. Perspectives on computational catalysis for metal nanoparticles. *ACS Catal.*, 9:8872–8881, 2019.

[84] F. Jensen. *Introduction to computational chemistry.* John Wiley & Sons Inc, 2007. ISBN 0470011874, 978-0470011874.

[85] M. R. Hestenes and E. Stiefel. Methods of conjugate gradients for solving linear systems. *Journal of Research of the National Bureau of Standards*, 49:409–436, 1952.

[86] G. Kresse and J. Hafner. Ab initio molecular dynamics for open-shell transition metals. *Phys. Rev. B*, 48:13115–13118, 1993.

[87] G. Kresse and J. Hafner. Ab initio molecular-dynamics simulation of the liquid-metal–amorphous-semiconductor transition in germanium. *Phys. Rev. B*, 49:14251–14269, 1994.

[88] K. Reuter and M. Scheffler. Composition, Structure, and Stability of RuO_2(110) as a Function of Oxygen Pressure. *Phys. Rev. B*, 65:035406, 2001.

[89] M. Scheffler. Thermodynamic Aspects of Bulk and Surface Defects - First-Principle Calculations -. *Stud. Surf. Sci. Catal.*, 40:115–122, 1988.

[90] Stanley I. Sandler. *An Introduction to Applied Statistical Thermodynamics*. Wiley, 2010. ISBN 0470913479, 978-0470913475.

[91] I. Chorkendorff and J.W. Niemantsverdriet. *Concepts of modern catalysis and kinetics*. Wiley, 2007. ISBN 978-3527316724.

[92] R. F. W. Bader. *Atoms in molecules: A quantum theory*. Oxford University Press, London, 1994.

[93] R.F. Bader. The zero-flux surface and the topological and quantum definitions of an atom in a molecule. *Theor. Chem. Acc*, 105:276–283, 2001.

[94] W. Tang, E. Sanville, and G. Henkelman. A grid-based bader analysis algorithm without lattice bias. *J. Phys.: Condens. Matter*, 21:084204, 2009.

[95] H. Öström, H. Öberg, H. Xin, J. LaRue, M. Beye, M. Dell'Angela, J. Gladh, M. L. Ng, J. A. Sellberg, S. Kaya, G. Mercurio, D. Nordlund, M. Hantschmann, F. Hieke, D. Kühn, W. F. Schlotter, G. L. Dakovski, J. J. Turner, M. P. Minitti, A. Mitra, S. P. Moeller, A. Föhlisch, M. Wolf, W. Wurth, M. Persson, J. K. Nørskov, F. Abild-Pedersen, H. Ogasawara, L. G. M. Pettersson, and A. Nilsson. Probing the Transition State Region in Catalytic CO Oxidation on Ru. *Science*, 347:978–982, 2015.

[96] G. Mills, H. Jónsson, and G. K. Schenter. Reversible work transition state theory: Application to dissociative adsorption of hydrogen. *Surf. Sci.*, 324:305—337, 1995.

[97] G. Henkelman and H. Jónsson. Improved tangent estimate in the nudged elastic band method for finding minimum energy paths and saddle points. *J. Chem. Phys.*, 113:9978–9985, 2000.

[98] G. Henkelman, B. P. Uberuaga, and H. Jónsson. A climbing image nudged elastic band method for finding saddle points and minimum energy paths. *J. Chem. Phys.*, 113:9901–9904, 2000.

[99] D. Frenkel and B. Smit. *Understanding molecular simulation*. Academic, 2002. ISBN 978-0-12-267351-1.

[100] R. N. Barnett, U. Landman, A. Nitzan, and G. Rajagopal. Born–oppenheimer dynamics using density-functional theroy: Equilibrium and fragmentation of small sodium clusters. *J. Chem. Phys.*, 94:608–616, 1991.

[101] R. Car and M. Parrinello. Unified Approach for Molecular Dynamics and Density-Functional Theory. *Phys. Rev. Lett.*, 55:2471–2474, 1985.

[102] W. C. Swope and H. C. Andersen. A computer simulation method for the calculation of equilibrium constants for the formation of physical clusters of molecules: Application to small water clusters. *J. Chem. Phys.*, 76:637–649, 1982.

[103] S. Nosé. A unified formulation of the constant temperature molecular dynamics methods. *J. Chem. Phys.*, 81:511–519, 1984.

[104] S. Nosé. A molecular dynamics method for simulations in the canonical ensemble. *Mol. Phys.*, 52:255–268, 1984.

[105] W. G. Hoover. Canonical dynamics: equilibrium phase-space distributions. *Phys. Rev. A*, 31:1695–1697, 1985.

[106] M. Sprik. Free energy from constrained molecular dynamics. *J. Chem. Phys.*, 109: 7737–7744, 1998.

[107] E. A. Carter, G. Ciccotti, J. T. Hynes, and R. Kapral. Constrained Reaction Coordinate Dynamics for the Simulation of Rare Events. *Chem. Phys. Lett.*, 156: 472–477, 1989.

[108] G. Centi, S. Perathoner, F. Trifiro, A. Aboukais, C.F. Aissi, and M. Guelton. Physicochemical characterization of V-silicalite. *J. Phys. Chem.*, 96:2617–2629, 1992.

[109] F. Lónyi and J. Valyon. On the interpretation of the NH_3-TPD patterns of H-ZSM-5 and H-mordenite. *Microporous Mesoporous Mater.*, 47:293–301, 2001.

[110] K.A. Lomachenko, E. Borfecchia, C. Negri, G. Berlier, C. Lamberti, P. Beato, H. Falsig, and S. Bordiga. The Cu-CHA deNO_x catalyst in action: Temperature-dependent NH_3-assisted selective catalytic reduction monitored by operando XAS and XES. *J. Am. Chem. Soc.*, 138:12025–12028, 2016.

[111] L. Chen, T.V.W. Janssens, M. Skoglundh, and H. Grönbeck. Interpretation of NH_3-TPD profiles from Cu-CHA using first-principles calculations. *Top. Catal.*, 62: 93–99, 2019.

[112] A. K. S. Clemens, A. Shishkin, P.-A. Carlsson, M. Skoglundh, Z. Matěj F. J. Martínez-Casado, O. Balmes, and H. Härelind. Reaction-driven ion exchange of copper into zeolite SSZ-13. *ACS Catal.*, 5:6209–6218, 2015.

[113] A. Clearfield. Crystal Structure of Chabazite, A Molecular Sieve. *Chern. Rev.*, 88: 125–148, 1988.

[114] E. Kikuchi, M. Ogura, I. Terasaki, and Y. Goto. Selective Reduction of Nitric Oxide with Methane on Gallium and Indium Containing H-ZSM-5 Catalysts: Formation of Active Sites by Solid-State Ion Exchange. *J. Catal.*, 161:1794–1796, 1996.

[115] M. Zamadics, X.H. Chen, and L. Kevan. Solid-State Ion Exchange in H-SAPO-34: Electron Spin Resonance and Electron Spin Echo Modulation Studies of Copper (II) Location and Adsorbate Interaction. *J. Phys. Chem.*, 96:5488–5491, 1992.

[116] F. Gao, E. D. Walter, N. M. Washton, J. Szanyi, and C. H. Peden. Synthesis and Evaluation of Cu/SAPO-34 Catalysts for NH_3-SCR 2: Solid-State Ion Exchange and One-Pot Synthesis. *Appl. Catal., B*, 162:501–514, 2015.

[117] S. Shwan, M. Skoglundh, L.F. Lundegaard, R.R. Tiruvalam, T.V. Janssens, A. Carlsson, and P.N. Vennestrøm. Solid-state ion-exchange of copper into zeolites facilitated by ammonia at low temperature. *ACS Catal.*, 5:16–19, 2015.

[118] L.I. Bendavid and E.A. Carter. First-principles predictions of the structure, stability, and photocatalytic potential of Cu_2O surfaces. *J. Phys. Chem. B*, 117:15750–15760, 2013.

[119] K. Leistner, K. Xie, A. Kumar, K. Kamasamudram, and L. Olsson. Ammonia desorption peaks can be assigned to different copper sites in Cu/SSZ-13. *Catal. Lett.*, 147:1882–1890, 2017.

[120] J. Luo, F. Gao, K. Kamasamudram, N. Currier, C.H. Peden, and A. Yezerets. New insights into Cu/SSZ-13 SCR catalyst acidity. Part I: Nature of acidic sites probed by NH_3 titration. *J. Catal.*, 348:291–299, 2017.

[121] F. Gao, N.M. Washton, Y. Wang, M. Kollár, J. Szanyi, and C.H. Peden. Effects of Si/Al ratio on Cu/SSZ-13 NH_3-SCR catalysts: Implications for the active Cu species and the roles of Brønsted acidity. *J. Catal.*, 331:25–38, 2015.

[122] T. Zhang, F. Qiu, H. Chang, X. Li, and J. Li. Identification of active sites and reaction mechanism on low-temperature scr activity over cu-ssz-13 catalysts prepared by different methods. *Catal. Sci. Technol.*, 6:6294–6304, 2016.

[123] L. Rodríguez-González, F. Hermes, M. Bertmer, E. Rodríguez-Castellón, A. Jiménez-López, and U. Simon. The acid properties of H-ZSM-5 as studied by NH_3-TPD and ^{27}Al-MAS-NMR spectroscopy. *Appl. Catal., A*, 328:174–182, 2007.

[124] S.A. Bates, A.A. Verma, C. Paolucci, A.A. Parekh, T. Anggara, A. Yezerets, W.F. Schneider, J.T. Miller, W.N. Delgass, and F.H. Ribeiro. Identification of the active cu site in standard selective catalytic reduction with ammonia on cu-ssz-13. *J. Catal.*, 312:87–97, 2014.

[125] F. Gao, E.D. Walter, M. Kollar, Y. Wang, J. Szanyi, and C.H. Peden. Understanding ammonia selective catalytic reduction kinetics over Cu/SSZ-13 from motion of the Cu ions. *J. Catal.*, 319:1–14, 2014.

[126] B. Hammer, L.B. Hansen, and J.K. Nørskov. Improved adsorption energetics within density-functional theory using revised Perdew-Burke-Ernzerhof functionals. *Phys. Rev. B*, 59:7413–7421, 1999.

[127] J. Wellendorff, T.L. Silbaugh, D. Garcia-Pintos, J.K. Nørskov, T. Bligaard, F. Studt, and C.T. Campbell. A benchmark database for adsorption bond energies to transition metal surfaces and comparison to selected DFT functionals. *Surf. Sci.*, 640:36–44, 2015.

[128] L. Wang, T. Maxisch, and G. Ceder. Oxidation energies of transition metal oxides within the GGA + U framework. *Phys. Rev. B*, 73:195107, 2006.

[129] J. Yan, J.S. Hummelshøj, and J.K. Nørskov. Formation energies of group I and II metal oxides using random phase approximation. *Phys. Rev. B*, 87:075207, 2013.

[130] T.J. Goncalves, P.N. Plessow, and F. Studt. On the accuracy of density functional theory in zeolite catalysis. *ChemCatChem*, 11:4368–4376, 2019.

[131] L. Chen, H. Falsig, J. Jansson, T.V.W. Janssens, M. Skoglundh, and H. Grönbeck. Effect of Al-distribution on oxygen activation over Cu-CHA. *Catal. Sci. Technol.*, 8:2131–2136, 2018.

[132] L.Y. Isseroff and E.A. Carter. Importance of reference Hamiltonians containing exact exchange for accurate one-shot GW calculations of Cu_2O. *Phys. Rev. B*, 85: 235142, 2012.

[133] Y. Wang, S. Lany, J. Ghanbaja, Y. Fagot-Revurat, Y.P. Chen, F. Soldera, D. Horwat, F. Mücklich, and J.F. Pierson. Electronic structures of Cu_2O, Cu_4O_3, and CuO: A joint experimental and theoretical study. *Phys. Rev. B*, 94:245418, 2016.

[134] C.J. Cramer, B.A. Smith, and W.B. Tolman. Ab initio characterization of the isomerism between the μ–η^2:η^2–peroxo– and bis(μ–oxo)dicopper cores. *J. Am. Chem. Soc.*, 118:11283–11287, 1996.

[135] C.J. Cramer, M. Włoch, P. Piecuch, C. Puzzarini, and L. Gagliardi. Theoretical models on the Cu_2O_2 torture track: Mechanistic implications for oxytyrosinase and small–molecule analogues. *J. Phys. Chem. A*, 110:1991–2004, 2006.

[136] C.J. Cramer, A. Kinal, M. Włoch, P. Piecuch, and L. Gagliardi. Theoretical characterization of end-on and side-on peroxide coordination in ligated Cu_2O_2 models. *J. Phys. Chem. A*, 110:11557–11568, 2006.

[137] L. Noodleman. Valence bond description of antiferromagnetic coupling in transition metal dimers. *J. Chem. Phys.*, 74:5737–5743, 1981.

[138] R. Valero, R. Costa, I. de PR Moreira, D.G. Truhlar, and F. Illas. Performance of the M06 family of exchange-correlation functionals for predicting magnetic coupling in organic and inorganic molecules. *J. Chem. Phys.*, 128:114103, 2008.

[139] P. Rivero, C. Loschen, I.D.P. Moreira, and F. Illas. Performance of plane-wave-based LDA + U and GGA + U approaches to describe magnetic coupling in molecular systems. *J. Comput. Chem.*, 30:2316–2326, 2009.

[140] H. Falsig, P.N.R. Vennestrøm, P.G. Moses, and T.V.W. Janssens. Activation of oxygen and NO in NH_3-SCR over Cu-CHA catalysts evaluated by density functional theory. *Catal. Today*, 59:861–865, 2016.

[141] F. Göltl, R.E. Bulo, J. Hafner, and P. Sautet. What makes copper-exchanged SSZ-13 zeolite efficient at cleaning car exhaust gases? *J. Phys. Chem. Lett.*, 4: 2244–2249, 2013.

[142] U. Deka, A. Juhin, E.A. Eilertsen, H. Emerich, M.A. Green, S.T. Korhonen, B.M. Weckhuysen, and A.M. Beale. Confirmation of isolated cu^{2+} ions in ssz-13 zeolite as active sites in nh_3-selective catalytic reduction. *J. Phys. Chem. C*, 116:4809–4818, 2012.

[143] E. Borfecchia, C. Negri, K.A. Lomachenko, C. Lamberti, T.V.W. Janssens, and G. Berlier. Temperature-dependent dynamics of NH_3-derived Cu species in the Cu-CHA SCR catalyst. *React. Chem. Eng.*, 4:1067–1080, 2019.

[144] F. Gao, E. D. Walter, E. M. Karp, J. Luo, R. G. Tonkyn, J. H. Kwak, J. Szanyi, and C. H. Peden. Structure-activity relationships in NH_3-SCR over Cu-SSZ-13 as probed by reaction kinetics and EPR studies. *J. Catal.*, 300:20–29, 2013.

[145] M. Sun, J. Liu, C. Song, Y. Ogata, H. Rao, X.Q. Zhao, H. Xu, and Y.Q. Chen. The different reaction mechanisms of ammonia oxidation reaction on Pt/Al_2O_3 and $Pt/CeZrO_2$ with various Pt states. *ACS Appl. Mater. Interfaces*, 11:23102–23111, 2019.

[146] M. Colombo, I. Nova, and E. Tronconi. A comparative study of the NH_3-SCR reactions over a Cu-zeolite and a Fe-zeolite catalyst. *Catal. Today*, 151:223–230, 2010.

[147] L. Olsson, H. Sjövall, and R.J. Blint. A kinetic model for ammonia selective catalytic reduction over Cu-ZSM-5. *Appl. Catal. B - Environ.*, 81:203–217, 2008.

[148] P.S. Metkar, M.P. Harold, and V. Balakotaiah. Experimental and kinetic modeling study of NH_3-SCR of NO_x on Fe-ZSM-5, Cu-chabazite and combined Fe-and Cu-zeolite monolithic catalysts. *Chem. Eng. Sci.*, 87:51–66, 2013.

[149] A. Grossale, I. Nova, E. Tronconi, D. Chatterjee, and M. Weibel. The chemistry of the NO/NO_2–NH_3 "fast" SCR reaction over Fe-ZSM-5 investigated by transient reaction analysis. *J. Catal.*, 256:312–322, 2008.

[150] M. Devadas, O. Kröcher, M. Elsener, A. Wokaun, N. Söger, M. Pfeifer, Y. Demel, and L. Mussmann. Influence of NO_2 on the selective catalytic reduction of NO with ammonia over Fe-ZSM-5. *Appl. Catal. B - Environ.*, 67:187–196, 2006.

[151] A. Grossale, I. Nova, E. Tronconi, D. Chatterjee, and M. Weibel. NH_3–NO/NO_2 SCR for diesel exhausts aftertreatment: Reactivity, mechanism and kinetic modelling of commercial Fe-and Cu-promoted zeolite catalysts. *Top. Catal.*, 52:1837–1841, 2009.

[152] Y. Cui and F. Gao. Cu Loading Dependence of Fast NH_3-SCR on Cu/SSZ-13. *Emiss. control sci. technol.*, 5:124–132, 2019.

[153] N. Metropolis, A.W. Rosenbluth, M.N. Rosenbluth, A.H. Teller, and E. Teller. Equation of state calculations by fast computing machines. *J. Chem. Phys.*, 21: 1087–1092, 1953.

[154] D.J. Wales and J.P. Doye. Global optimization by basin-hopping and the lowest energy structures of Lennard-Jones clusters containing up to 110 atoms. *J. Phys. Chem. A*, 101:5111–5116, 1997.

[155] G. Bussi, A. Laio, and M. Parrinello. Equilibrium free energies from nonequilibrium metadynamics. *Phys. Rev. Lett.*, 96:090601, 2006.

[156] C. Loschen, J. Carrasco, K.M. Neyman, and F. Illas. First-principles LDA + U and GGA + U study of cerium oxides: dependence on the effective U parameter. *Phys. Rev. B*, 75:035115, 2007.

[157] M. Nielsen, R.Y. Brogaard, H. Falsig, P. Beato, O. Swang, and S. Svelle. Kinetics of zeolite dealumination: insights from H-SSZ-13. *ACS Catal.*, 5:7131–7139, 2015.

[158] M. Jørgensen, L. Chen, and H. Grönbeck. Monte Carlo potential energy sampling for molecular entropy in zeolites. *J. Phys. Chem. C*, 122:20351–20357, 2018.

[159] G. Piccini and J. Sauer. Quantum chemical free energies: Structure optimization and vibrational frequencies in normal modes. *J. Chem. Theory Comput.*, 9:5038–5045, 2013.

[160] G. Piccini, M. Alessio, and J. Sauer. Ab initio calculation of rate constants for molecule–surface reactions with chemical accuracy. *Angew. Chem. Int. Ed.*, 55: 5235–5237, 2016.

[161] G. Piccini, M. Alessio, and J. Sauer. Ab initio study of methanol and ethanol adsorption on Brønsted sites in zeolite H-MFI. *Phys. Chem. Chem. Phys.*, 20: 19964–19970, 2018.